PROCEEDINGS A

rspa.royalsocietypublishing.org

Research

Article submitted to journal

Subject Areas:
aeroacoustics, applied mathematics

Keywords:
asymptotics, cone of silence, complex rays, caustics, Lilley's equation, subsonic aeroacoustics

Author for correspondence:
J. T. Stone
e-mail: J.T.Stone@soton.ac.uk
C. J. Howls
e-mail: C.J.Howls@soton.ac.uk

THE ROYAL SOCIETY
PUBLISHING

Aeroacoustic catastrophes: upstream cusp beaming in Lilley's equation

J. T. Stone[1,2], R. H. Self[1] and C. J. Howls[2]

[1]Institute of Sound and Vibration Research, University of Southampton, Highfield, Southampton, SO17 1BJ, UK

[2]Mathematical Sciences, University of Southampton, Highfield, Southampton, SO17 1BJ, UK

The downstream propagation of high-frequency acoustic waves from a point source in a subsonic jet obeying Lilley's equation is well known to be organised around the so called "cone of silence", a fold catastrophe across which the amplitude may be modelled uniformly using Airy functions. Here we show that not only do acoustic waves unexpectedly propagate upstream, but are also organised at constant distance to the point source around a cusp catastrophe with amplitude modelled locally by the Pearcey function. Furthermore the cone of silence is revealed to be a cross-section of a swallowtail catastrophe. One consequence of these discoveries is that the peak acoustic field upstream is not only structurally stable but also at a similar level to the known downstream field. The fine structure of the upstream cusp is blurred out by distributions of symmetric acoustic sources, but peak upstream acoustic beaming persists when asymmetries are introduced, either from arrays of discrete point sources or perturbed continuum ring source distributions. These results may pose interesting questions for future novel jet-aircraft engine designs where asymmetric source distributions arise.

1. Introduction

Over the past 60 years, much research into the acoustic pressure field arising from jet flow has been based on the acoustic analogy originally developed by Lighthill [**?**,**?**] and later extended by Lilley [**?**]. The Lilley analogy models the acoustic field due to fine-scale turbulence in a subsonic jet by propagating the acoustic field of equivalent multipole-type convected compact sources through a mean parallel shear flow, [**?**]. This allows a

close approximation of the acoustic field from slowly spreading subsonic jets, facilitating the reduction of the governing propagation equations to a single 3rd order linear wave equation - Lilley's equation.

In the subsonic regime the linearity of the Lilley equation may be exploited by constructing a Green function which describes the flow-acoustic interaction effects from a simple monopole source. The total sound field at a particular frequency is then determined by convolving the Green function with a specified source distribution, [**?**].

Even in the flow geometries where the Green function is separable, its numerical determination is non-trivial. However, where the wavelength of propagation from a compact acoustic source is much smaller than the scales of the mean flow (as is the case within a few diameters of a round jet nozzle where turbulence is at its peak) a high-frequency approach may facilitate the calculation. Though the approximate cross-over to this regime will differ depending on the flow, such solutions have been shown for subsonic single stream parallel jets to agree with numerical computation down to Strouhal numbers of 1 by Tester and Morfey [**?**] and more recently as low as a $1/2$ by Wundrow and Khavaran [**?**].

In the case of high-frequency propagation, there are two popular asymptotic approaches. First, when the flow is radially symmetric an approximation of the Green function by separation of variables leads to a series of truncated Fourier modes each containing a leading order WKB expansion in the large wavenumber (see [**?**], [**?**,**?**]). A first term approximation of this sum forms the well-known MGB method due to Mani *et al.* [**?**]. However, abandoning non-zeroth mode terms oversimplifies the acoustics by losing information regarding the directional behaviour of jet noise. In this paper we show that retaining these terms is vital to an accurate calculation of the directivity of the Green function 3D free space.

Alternatively the Green function may be described using ray theory or geometrical acoustics (see [**?**,**?**]). Recent developments have shown that one can now seek full-scale ray solutions to the Green function field in a generic flow (see [**?**,**?**]), including the important effects of complex-rays, [**?**]. The trade-off between a computationally efficient symmetric WKB expression and a full asymmetric solution is not automatically required [**?**,**?**]. In those papers we provide a practical numerical algorithm to calculate acoustic fields in the presence of generic subsonic flows (symmetric or asymmetric), using both real and complex rays. We exploit that machinery here to give a glimpse of the rich underpinning mathematical structures of the acoustic field from a point source.

Much of the previous work for subsonic jets using the linearised Lilley's equation considers the Green function in the far-field downstream of a point source. The downstream region of the jet contains the acoustic "cone of silence" (see [**?**], [**?**]), the shadow zone of the high-frequency Green function. The field within the cone of silence is generated from complex rays only. It is delineated from the rest of the acoustic field by a region of peak amplitude.

Near to the loci of the peak acoustic field, the ray approximations generate a singular, divergent amplitude. This is due to the tangency of pairs of rays emitted from the point source [**?**] causing the vanishing of a Jacobian [**?**,**?**] in the denominator of the local approximation. The effective boundary of the cone of silence is thus a fold caustic of the rays, being the simplest member of the catastrophe hierarchy of bifurcation sets (see [**?**], chapter 36 of [**?**], [**?**,**?**]). It is well known that the field across this fold catastrophe may be uniformly approximated using Airy functions, [**?**,**?**].

In this paper we initially consider the far-field Green function of a point source in a typical subsonic jet flow in a high-frequency (high-Strouhal number) limit using ray approximations in all three dimensional directions. Importantly we include both upstream and downstream analysis. We restrict our analysis to subsonic flows governed by ideal and perfect gas laws and do not consider instability or shock associated noise that requires a partial or full nonlinear treatment.

We find that the downstream fold catastrophe is complemented by a region of peak noise extending forward from an off-axis point source in the flow, in an upstream direction. The intersection of the associated caustic of rays with the surface of a far-field sphere centred on the point source is a cusp. The cusp is formed by three interacting real rays and is the next most

complicated caustic in the hierarchy of catastrophe theory. We show that a uniform approximation of the Green function generates an upstream field amplitude comparable in magnitude to that of the downstream fold catastrophe. For a point source, the cusp is decorated by rapid oscillations of the Green function caused by interferences of the three real rays, uniformly approximated locally by Pearcey functions, [**?**].

Whilst upstream beaming of supersonic screech and broadband noise is well established (see [**?**,**?**]) this involves fundamentally different mechanisms to those discussed in this paper. For subsonic flows emanating from round jets with symmetric source distributions, upstream beaming is non-existent [**?**] and the downstream sound pressure levels dominate angular spectra. However, if an asymmetry is present in the source distribution then upstream beaming may appear. Some indications of the upstream beaming we observe here may be found in the theoretical and experimental results of Powles & Tester [**?**] wherein the shielding effects of a subsonic jet were studied by artificially generating a monopole noise source external to the flow. However, the upstream angular range they cover and the experimental sampling frequency within that range is limited. Hence they do not cover the entire domain where the full complexity of the upstream structures that we have calculated here are revealed.

It should be emphasised that we study a fully 3D system in the absence of boundaries. The present structure contrasts with previous appearances of cusps in aeroacoustic problems: e.g., [**?**], where caustics are focused downstream in subsonic flows and formed by rays reflecting off 2D boundaries, [**?**], where cusps are embedded in hyperbolic umbilic catastrophes inside ducts caused by edge diffraction, or in supersonic flows by the focussing of 2D supersonic shock waves, [**?**], and to model downstream shock cells in jets, [**?**].

Although the downstream acoustic field has been well studied (see [**?**,**?**,**?**]), our analysis illustrates additional novel structures within that regime. The fold catastrophe itself is actually embedded within a swallowtail catastrophe, the appearance of which is controlled by the radial source distance from the jet centreline. This is the third most complicated structure in the catastrophe hierarchy, [**?**]. The local form is of further mathematical interest since it arises from the interaction of four rays, but unusually two of which are complex.

As members of the catastrophe theory hierarchy these caustics are structurally stable, i.e., resistant to perturbations. They can therefore be assumed to be present for a generic range of parameters. We show elsewhere the cusp persists for a range of subsonic Mach numbers, [**?**].

However, this is not the complete story, as any realistic acoustic field modelled by the linear Lilley analogy may be approximated as the sum of a distribution of such point sources, [**?**]. For asymmetric discrete and continuous distributions we show that although the fine structure oscillations in the Green function are washed out, the catastrophe structures generating local peaks of field-amplitude still visibly persist in the field. Such washing is also likely to occur in other realistic scenarios.

The outline of the paper is as follows. In section **??**, we revisit the high-frequency modal solution of Wundrow & Khavaran [**?**], the standard numerical testbed for point-source off-axis jet noise. Extending the modal solution to account for more complicated turning-point structures, we plot a global solution (section **??**) to reveal the catastrophe structure using a prototypical axisymmetric jet profile. In section **??** we begin our analysis of the cusp catastrophe in the upstream direction. Ray trajectories are visualised and classified according to the Poisson summation method of [**?**]. Analysis then moves onto the downstream region in section **??** whereby a local diffraction integral is derived to describe the cone of silence boundary, resolving ray conservation issues found in [**?**,**?**]. The final sections of this paper consider the impact of both upstream and downstream singularities, starting with a direct magnitude and energy calculation in section **??**, and culminating with a source distribution study based on correlation integrals in section **??**.

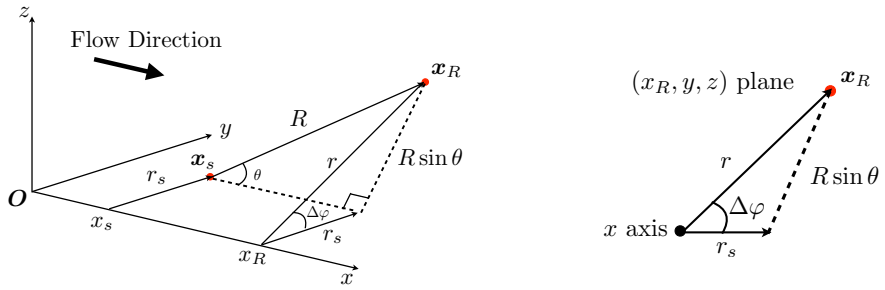

(a) Global coordinates

(b) x_R-plane coordinates.

Figure 1: Cylindrical and spherical coordinates for flow and receiver respectively.

2. Green function solution

In this section we present the modal Green function solution to Lilley's equation, based on an extension to Wundrow & Kharavan [**?**]. Although this solution relies on separable flow it nevertheless acts as a benchmark for our more general ray analysis.

The parallel shear flow configuration specifies an infinitely long cylindrical jet according to the flow profiles

$$\bar{\boldsymbol{u}} = \mathbf{i}\bar{u}_1(r) = \mathbf{i}\bar{c}_\infty M(r), \quad \bar{c}(r) = \bar{c}_\infty a(r), \quad \bar{\rho}(r), \tag{2.1}$$

where $\bar{\boldsymbol{u}}$, $\bar{c}$, and $\bar{\rho}$ are the mean velocity, sound speed and density, respectively, and $M(r)$ and $a(r)$ the acoustic Mach number and sound speed ratio, respectively. All profiles are functions of the radial coordinate $r = \sqrt{y^2 + z^2}$ specified in the Cartesian coordinate system (x, y, z) of figure **??**, so that $\bar{u}_1$, the downstream flow, is aligned with the x-axis with $\mathbf{i}$ the unit vector in that direction. Variables (**??**) take on ambient values $\bar{u}_1 \to 0$, $\bar{c} \to \bar{c}_\infty$, $\bar{\rho} \to \bar{\rho}_\infty$ as $r \to +\infty$.

As in [**?**] for computational convenience we consider two Green function solutions of Lilley's equation given by

$$\mathscr{L}_L \mathbb{G}_\omega = \bar{c}_\infty^2 \delta(\boldsymbol{x}_R - \boldsymbol{x}_s), \qquad \mathscr{L}_L G_\omega = \bar{c}_\infty^2 \bar{D}_\omega \delta(\boldsymbol{x}_R - \boldsymbol{x}_s), \tag{2.2, 2.3}$$

where the linearised time-harmonic Lilley operator in the characteristic angular frequency ω is defined as

$$\mathscr{L}_L \equiv \bar{D}_\omega \left(\bar{D}_\omega^2 - \nabla \cdot \bar{c}^2 \nabla \right) + 2\bar{c}^2 \frac{\mathrm{d}\bar{u}_1}{\mathrm{d}r} \frac{\partial^2}{\partial x \partial r}, \tag{2.4}$$

∇ the gradient operator in cylindrical coordinates (x, r, φ), and $\bar{D}_\omega \equiv -\mathrm{i}\omega + \bar{u}_1 \partial/\partial x$ the convective derivative. The coordinate geometry for a specific receiver $\boldsymbol{x}_R = (x, r, \Delta\varphi)$ and point source $\boldsymbol{x}_s = (x_s, r_s, \varphi_s)$ is shown in figure **??**,

$$\begin{gathered} \Delta\varphi = \varphi - \varphi_s = \arctan((z - z_s)/(y - y_s)), \\ R = \sqrt{(x - x_s)^2 + (y - y_s)^2 + (z - z_s)^2}, \quad \theta = \arccos((x - x_s)/R), \end{gathered} \tag{2.5}$$

where we set $\varphi_s = 0$ for single source computations without loss of generality.

The solution proceeds by determining G_ω first, then obtaining the ultimate solution $\mathbb{G}_\omega$ using the relation $G_\omega = -(\mathrm{i}\omega + \bar{u}_{s_1}\partial_{x_s})\mathbb{G}_\omega$. Noting the invariance of the Lilley operator in x and periodic nature of the field in $\Delta\varphi$ makes a combined Fourier transform-series in axial

wavenumber k_1 and azimuthal index n possible

$$G_\omega(\boldsymbol{x}_R|\boldsymbol{x}_s) = \frac{1}{4\pi^2}\sum_{n=-\infty}^{+\infty} \mathrm{e}^{\mathrm{i}n\Delta\varphi}\int_{-\infty}^{+\infty} G_n(r|r_s;\omega,k_1)\mathrm{e}^{-\mathrm{i}k_1(x-x_s)}\,\mathrm{d}k_1, \tag{2.6}$$

where the Fourier coefficients G_n satisfy the reduced equation

$$\frac{\Phi^2}{r}\frac{\mathrm{d}}{\mathrm{d}r}\left(\frac{r}{\Phi^2}\frac{\mathrm{d}}{\mathrm{d}r}G_n\right) + \left[k_0^2\left(\Phi^2-\kappa^2\right) - \frac{n^2}{r^2}\right]G_n = -\frac{\delta(r-r_s)}{r_s a_s^2}, \tag{2.7}$$

with $\Phi = (1+\kappa M(r))/a(r)$, $a_s = a(r_s)$, $\kappa = k_1/k_0$, and $k_0 = \omega/\bar{c}_\infty$ the characteristic wavenumber of propagation. The solution to (**??**) can be written down as (see Duffy [**?**])

$$G_n(r|r_s;\omega,k_1) = \frac{\Phi(r)}{\sqrt{r_s r}\,\Phi(r_s)}\frac{v_1(r_>|\kappa)v_2(r_<|\kappa)}{a_s^2\mathscr{W}(r_s|\kappa)}, \quad r \lessgtr r_s, \tag{2.8}$$

where $\mathscr{W}(r|\kappa) = v_1(r|\kappa)\frac{\mathrm{d}v_2(r|\kappa)}{\mathrm{d}r} - \frac{\mathrm{d}v_1(r|\kappa)}{\mathrm{d}r}v_2(r|\kappa)$ is the Wronskian and v_j $(j=1,2)$ is a solution to the homogeneous equation

$$\frac{\mathrm{d}^2 v_j}{\mathrm{d}r^2} + (k_0^2 Q_n^2 + \mathscr{I})v_j = 0, \tag{2.9}$$

where

$$rQ_n \equiv \sqrt{r^2q^2 - (n/k_0)^2}, \quad q \equiv \sqrt{\Phi^2-\kappa^2}, \quad \mathscr{I} \equiv \frac{\Phi}{r}\left(\frac{r}{\Phi^2}\frac{\mathrm{d}\Phi}{\mathrm{d}r}\right) + \left(\frac{1}{2r}\right)^2. \tag{2.10}$$

For far-field solutions we utilise the $r_>$ branch of (**??**) subject to the conditions

$$v_1(r|\kappa) \sim \mathrm{e}^{\mathrm{i}k_0\sqrt{1-\kappa^2}r}, \ r\to+\infty; \quad v_2(r|\kappa) \sim r^{1/2+|n|}, \ r\to 0, \tag{2.11}$$

which can be used to invert the Fourier transform in k_1 of (**??**) in the far-field regime, $R\to+\infty$, using the method of stationary phase, asymptotically evaluating the integral at the stationary point $k_1 = k_{1_\star} = k_0\kappa_\star$ (see Bleistein & Handelsman [**?**]). As shown in [**?**] this Fourier inversions leads to the solution of $\mathbb{G}_\omega$ as

$$\frac{\mathbb{G}_\omega(\boldsymbol{x}_R|\boldsymbol{x}_s)}{\mathscr{G}_\omega} = \frac{\mathrm{i}\mathscr{R}_\omega}{\bar{c}_\infty k_0 a_s^3\Phi_s^2}, \quad \mathscr{G}_\omega \equiv \frac{\mathrm{e}^{\mathrm{i}k_0R}}{4\pi R}, \quad \Phi_s = \Phi(r_s|-\cos\theta) = (1-M_s\cos\theta)/a_s, \tag{2.12}$$

$$\mathscr{R}_\omega \sim \sum_{n=-\infty}^{+\infty}\left(\frac{2k_0\sin\theta}{\mathrm{i}\pi r_s}\right)^{1/2}\frac{v_1(r|-\cos\theta)v_2(r_s|-\cos\theta)}{\mathscr{W}(r_s|-\cos\theta)}\mathrm{e}^{\mathrm{i}(n\Delta\varphi - k_0R\sin^2\theta)}, \tag{2.13}$$

where the stationary phase point $\kappa_\star = -\cos\theta$ has been used and is implicit from now on. It should also be noted that normalisation of $\mathbb{G}_\omega$ by $\mathscr{G}_\omega$ in (**??**) allows for a better interpretation of flow-acoustic interaction effects (see Tester and Morfey [**?**]).

The computation of $\mathbb{G}_\omega$ now depends on determining v_1 and v_2. Numerical routes are possible, however WKB solutions offer both a closed form estimation and our first glimpses at the inner workings of the point source field.

(a) WKB solutions

Solutions of (**??**) can be formed using the WKB method (see for e.g., Bender & Orszag [**?**], Heading [**?**]), neglecting $\mathscr{I}$ and expressing $v_{1,2}$ as linear combinations

$$v_j(s) \sim \sum_{i=1}^{2}\gamma_{ij}^{(k)}Q_n(s)^{-\frac{1}{2}}\exp\left((-)^i\mathrm{i}k_0\int_{r_{\delta_k}}^{s}Q_n(r')\,\mathrm{d}r'\right), \quad s = \begin{cases} r, & j=1, \\ r_s, & j=2. \end{cases} \tag{2.14}$$

Here r_{δ_k} is a reference turning-point, one of a number T real turning-points, which satisfy $Q_n(r_{\delta_k}) = 0$, ordered according to $r_{\delta_T} > r_{\delta_{T-1}} > \ldots > r_{\delta_1} \geq 0$. These turning-points partition the positive real line into subdomains. The solution in each subdomain is glued to the next using the connection constants $\gamma_{ij}^{(k)}$ (where (k) denotes the solution to the left of the r_{δ_k}-th turning-point). Turning-points are caustics of the modes, and their existence and position should not

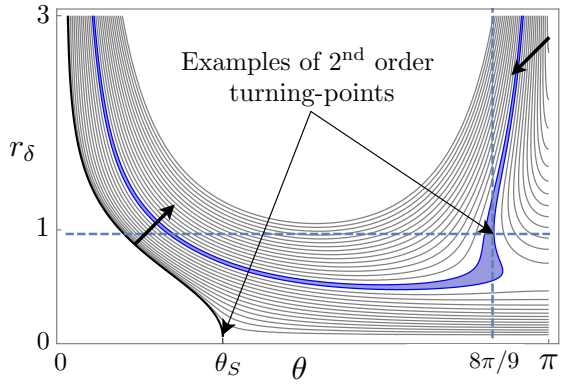

Figure 2: Roots r_δ of the function $Q_n(r_\delta)=0$, defined in (**??**), as a function of θ with flow $M(r)=M_J\mathrm{sech}^2(2r)$, $a(r)=1$, $M_J=0.9$, for modes $n\in[0,30]$. Thick black line, $n=0$ locus. Thick black arrows show increasing modal index. Blue lines highlight $n=14,15$. Blue dashed lines illustrate $\theta=\mathrm{const.}$ and its r_δ value. Second order turning-points at $\theta=\theta_S, 8\pi/9\,(160^\circ)$.

be confused with the ray caustics we analyse in later sections. From (**??**) we see that turning-points vary according to the flow (as q depends on Φ the function that characterises the flow), modal index n, wavenumber and receiver position θ (via the stationary point $\kappa_\star=-\cos\theta$). Even though the precise positions of the turning-points will differ depending on the precise form of Φ, the techniques which we use to deal with the turning-points will be the same.

For most $\theta\in[0,\pi)$, n in commonly used smooth subsonic flow profiles $a(r)$ and $M(r)$, there exists only one turning-point ($T=1$) on the positive real line (see [**?**]). For example, in figure **??** we show the root loci for the isothermal flow used in this paper: $M(r)=M_J\mathrm{sech}^2(2r)$, $M_J=0.9$, $a(r)=1$. By drawing a line of $\theta=\mathrm{const.}$ up to a particular modal curve, there is typically only one intersection, i.e., one turning-point. Consequently the most useful form is the simple turning-point problem, and for a large range of angles ($\theta<8\pi/9\,(160^\circ)$, $\theta\neq\theta_S$ for $n=0$, for the flow used here) one can use the results of [**?**] where the solutions of v_1, v_2 ($r>r_s,\ r\to+\infty$) are given as

$$v_1(r)\sim\gamma_{21}^{(2)}\mathrm{e}^{+\mathrm{i}k_0\zeta_n(r)},\quad v_2(r_s)\sim\gamma_{12}^{(1)}\left(\frac{4\pi\sqrt{-\eta_n^{(1)}(r_s)}}{Q_n(r_s)}\right)^{1/2}\mathrm{Ai}\left(\eta_n^{(1)}(r_s)\right),\qquad(2.15,\,2.16)$$

where Ai is the Airy function (see chapter 9, [**?**]), $\zeta_n(s)\equiv\int_{r_{\delta_1}}^{s}Q_n(r')\,\mathrm{d}r'$, and $\eta_n^{(1)}$ is defined via the function

$$\eta_n^{(m_{r_\delta})}(s)\equiv(-1)^{m_{r_\delta}}\left(\frac{m_{r_\delta}+2}{2}k_0\zeta_n(s)\right)^{2/(m_{r_\delta}+2)},\qquad(2.17)$$

with simple turning-point condition $m_{r_\delta}=1$ (see (**??**) and appendix **??**). This determines the Wronksian $\mathscr{W}\sim-2\mathrm{i}k_0\gamma_{21}^{(2)}\gamma_{12}^{(1)}\mathrm{e}^{\mathrm{i}\pi/4}$ which is constant.

The use of Ai on its own in (**??**) implies that it is "transitionally" uniform at r_{δ_1}, i.e., does not lead to a divergence in the modal field, but is the first term of the uniform expansion theory applicable to ordinary differential equations derived in appendix **??**. Numerically, we find these are appropriate for *modal* calculations even in the event of higher order turning-points.

In the event of higher-order and multiple turning-points we must amend (**??**) only, as $r\to+\infty$ of (**??**) means v_1 is never nonuniform at r_{δ_1}. These complicated turning-point geometries are not accounted for in the literature as they are typically found in upstream regions of the jet hitherto neglected. The exception to this is the higher-order turning-point in the $n=0$ mode for downstream θ discussed below. This occurs in a variety of subsonic jet flows (see [**?**,**?**,**?**]) and is key to understanding a new phenomenon presented in section **??**.

First, we deal with higher-order turning-points that occur in (**??**). For the flow regime used in this paper, figure **??** shows that there are two significant angular regions, $\theta = \theta_S$ for mode $n = 0$, and $\theta \geq 8\pi/9$ for modes $1 \leq n \leq 14$, where the turning-points become second order. For the angle θ_S this occurs due to a coalescence between a real positive turning-point and its image on the negative real axis, and those for $\theta > 8\pi/9$ occur due to a complex conjugate pair $r_{\delta_{2,3}}$ coalescing on the real line.

The second order turning-point structure at θ_S for $n = 0$ is easy to elicit from the local form of Q_n^2. Taylor expanding $q^2(r, \theta)$ about the turning-point at $r = 0$, noting that q^2 is even in r for this flow regime and truncating at second order gives

$$q^2(r, \theta) \sim T_0(\theta) + T_2(\theta) r^2, \tag{2.18}$$

where

$$T_0(\theta) \equiv 1 - 2M_J \cos\theta - \cos^2\theta + M_J^2 \cos^2\theta, \quad T_2(\theta) \equiv 8M_J \cos\theta - 8M_J^2 \cos^2\theta. \tag{2.19}$$

Now evaluating (**??**) at θ_S yields $T_0(\theta_S) = 0$, so that Q_n^2 has the local form

$$Q_n^2(r, \theta) \sim T_2(\theta) r^2 - \frac{(n/k_0)^2}{r^2}, \tag{2.20}$$

which is, for example, reminiscent of the potential used in a WKB approach to gravitational waves for a Schwarzschild black hole (see Andersson & Howls [**?**]), and leads us to label θ_S as the "Schwarzschild line". The second order turning-point exists in (**??**) when $n = 0$.

In both regions $\theta = \theta_S$ and $\theta \geq 8\pi/9$ we can use the local uniform form (**??**) from appendix **??** with second order condition $m_{r_\delta} = 2$ to determine the transitional solution. However for the modal problem, as opposed to ray analysis in section **??**, we use the alternative parabolic cylinder function representation of the relevant Bessel function (see appendix **??** and chapter 10.16 of [**?**])

$$\begin{aligned} v_2(r_s) \sim \gamma_{12}^{(1)} \mathrm{e}^{\pi \mathrm{i}/4} \left(\frac{\eta_n^{(2)}(r_s)}{Q_n(r_s)} \right)^{1/2} \Bigg[\left(\frac{1 - \sqrt{2}}{2^{1/4}} \right) \mathrm{e}^{3\pi \mathrm{i}/8} D_{-\frac{1}{2}} \left(\sqrt{2} \mathrm{e}^{-\pi \mathrm{i}/4} \eta_n^{(2)}(r_s) \right) + \\ \ldots - 2^{-1/4} \mathrm{e}^{-\pi \mathrm{i}/8} D_{-\frac{1}{2}} \left(-\sqrt{2} \mathrm{e}^{-\pi \mathrm{i}/4} \eta_n^{(2)}(r_s) \right) \Bigg]. \end{aligned} \tag{2.21}$$

For large angles $\theta > 8\pi/9$, multiple turning-points exist as a result of the complex conjugate pair of turning-points, $r_{\delta_{2,3}}$, scattering along the real axis post coalescence and introducing a new region of decay (unphysical growing solutions are discarded) between $r_{\delta_1} < r' < r_{\delta_2}$. This is shown in figure **??** as $\theta = \mathrm{const.}$ lines intersect the modal curves three times. In this case rather than derive a new solution we prefer to modify the simple turning-point solution utilising the $\eta_n^{(1)} \gg 1$ expansion of (**??**) as shown appendix **????**. In the following calculations we exclude the point $\theta = \pi$ as the infinite number of turning-points - corresponding to trapped rays [**?**] - lies beyond our modification.

3. Combined catastrophes

In this section we display the magnitude of the modal solution, $|\mathbb{G}_\omega / \mathscr{G}_\omega|$, of (**??**) as a function of $\Delta\varphi \in [0, 2\pi)$ and $\theta \in [0, \pi)$ for the first time. This reveals key information concerning the structures about which the whole field is organised. Figure **??** shows the modal solution for an isothermal jet, $a(r) = 1$, using flow profile $M(r) = M_J \operatorname{sech}^2(2r)$, $M_J = 0.9$, source point $\boldsymbol{x}_s = (0, 0.75, 0)$, and far-field radius $R = 200$. The field is expressed in terms of both Strouhal number $St = k_0 r_J / \pi a(0) M_J$ with $r_J = 1/2$, $a(0) = 1$, and wavenumber k_0. As in [**?**] a modal criterion of $n_{\max} = O(k_0 r_s)$ is used to truncate (**??**), replacing limits $n = \pm\infty$ by $n = \pm n_{\max}$.

The modal field (**??**) shown in figure **??** for this particular subsonic flow is typical of off-axis source positions, $r_s > 0$. Figure **??** also exhibits the benefits of a 2D plot with extended plot range as opposed to constant $\Delta\varphi$ cross-sections shown in [**?**]. It is now clear from the diffraction patterns

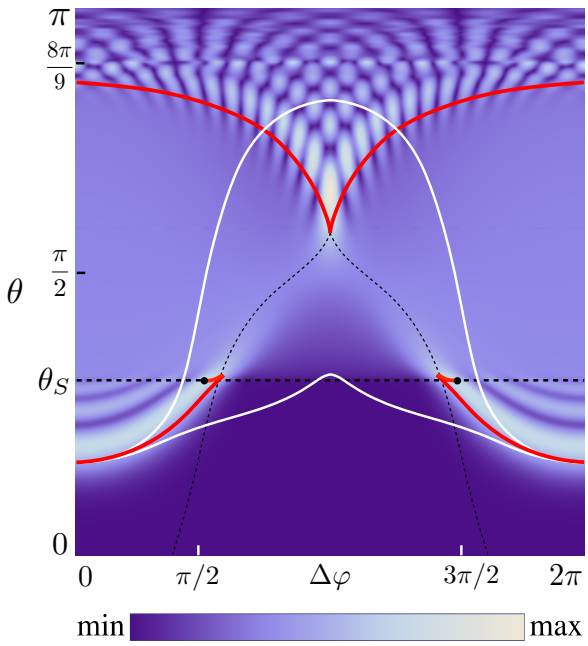

Figure 3: $|\mathbb{G}_\omega/\mathscr{G}_\omega|$ with ray structures overlaid ($St = 5$, $k_0 = 28.27$, $r_s = 0.75$). Red lines, caustics; thin dashed line, Stokes set; thick dashed line, Schwarzschild line θ_S; white line, ray delimiter (see section **??**); black points, caustic evaporation points.

alone that $\mathbb{G}_\omega$ possesses a rich variety of structures which we shall show are members of the catastrophe theory hierarchy.

We can locate the caustic structures that organise these diffraction patterns by using the ray tracing apparatus of [**?**,**?**]. The caustics, where the ray amplitude is singular, can be located by calculating the loci of points where the ray Jacobians vanish. The local catastrophe forms can be deduced by counting the number of singular rays involved at the caustic.

As figure **??** shows there are two caustics inhabiting two distinct regions of the field, a fact reinforced by the spherical polar plots of figure **??**. The first in the downstream region, $\theta < \pi/2$, organises the diffraction pattern delimiting the cone of silence - the region of exponential attenuation existing for low polar angles (see also [**?**]). To date this has been classified as a fold caustic, controlled and decorated locally by the Airy function. This last fact is easy to see when we correct for ray non-uniformity using the local form

$$\mathbb{G}_\omega \sim (2\pi)^{1/2} k_0^{-5/6} c_{0,0} \mathrm{e}^{\mathrm{i}(k_0 A_{CE} - \frac{\pi}{4})} \mathrm{Ai}(k_0^{2/3}\xi_1), \tag{3.1}$$

where A_{CE} and $c_{0,0}$ are analogous to the ray phase and amplitude, and critically ξ_1 controls the essentially one dimensional oscillations. The local form (**??**) is analogous to, but distinct from, (**??**) used to provide uniformity in the modes.

Under the ray approximation the scenario is simple: two real/complex rays coalesce together (or are tangential in physical space) violently at the caustic giving birth to a complex/real ray pair in a manner equivalent to the bifurcations of two polynomial roots. However, as we shall show in section **??** of this paper this caustic is more than just a fold. There are two peculiarities suggesting otherwise: first, existence of caustic evaporations point where the caustic appears to disappear from the field; second, apparent cusp-like kinks just visible in figure **??** above $\theta = \theta_S$ near to $\Delta\varphi = \pi/2, 3\pi/2$. As we show in section **??**, these kinks are dependent on source parameters.

The second caustic of $\mathbb{G}_\omega$, the cusp, inhabits the upstream or "against the flow" region, $\theta > \pi/2$, and sees us reap the rewards of retaining non-zeroth modal terms in (**??**). The cusp, a new

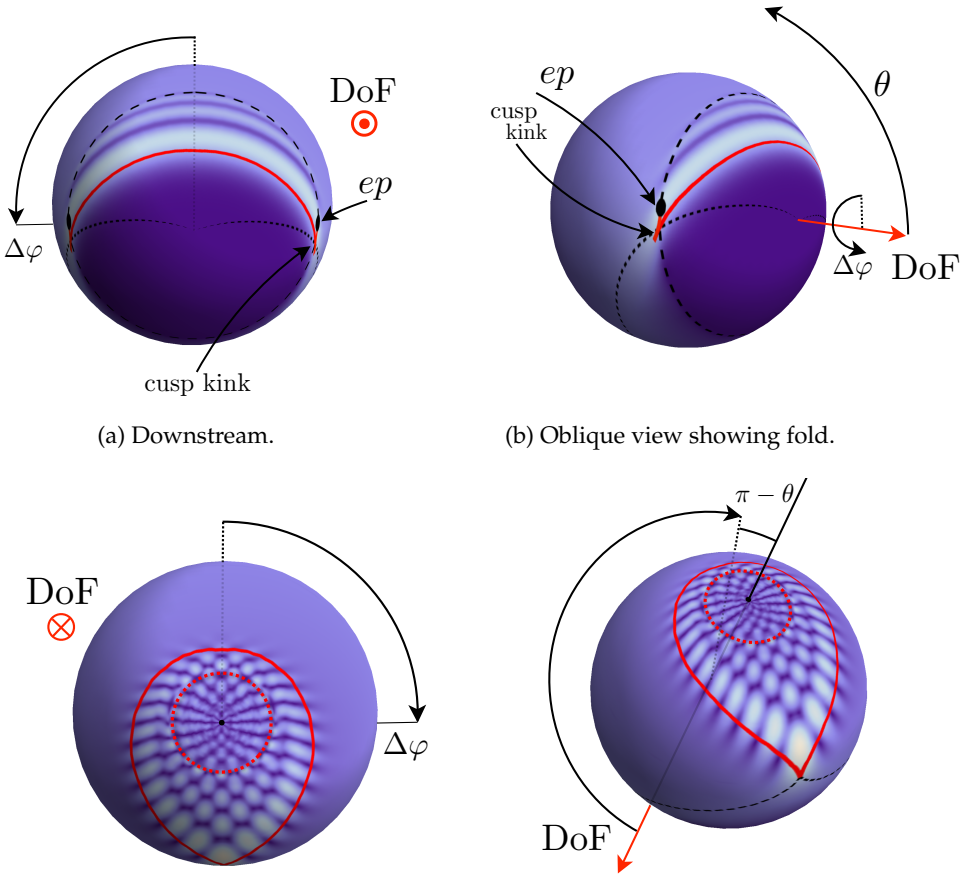

(a) Downstream.

(b) Oblique view showing fold.

(c) Upstream.

(d) Oblique view showing cusp.

Figure 4: $|\mathbb{G}_\omega/\mathscr{G}_\omega|$ of figure **??** plotted in $(R, \Delta\varphi, \theta)$ space with ray delimeter removed. A red dashed line is added to (c) & (d) indicating the three turning-point regime for $\theta \geq 8\pi/9\,(160^\circ)$. DoF, direction of flow. Electronic materials attached allow reader to change viewpoint.

discovery of $\mathbb{G}_\omega$, is formed due to the tangency and interference of a ray triplet and is decorated locally by the Pearcey function, P (see equation 36.2.14, [**?**]). We can show this as before by evaluating the uniform expansion for the case of three rays

$$\mathbb{G}_\omega \sim \pi^{-1/2} k_0^{-3/4} c_{0,0} \mathrm{e}^{\mathrm{i}(k_0 A_{CE} - \frac{\pi}{4})} P(2^{1/2} k_0^{3/4} \xi_1, k_0^{1/2} \xi_2). \tag{3.2}$$

Here, $c_{0,0}$ and A_{CE} are as before - though take on different numerical values - and the presence of two control variables $\xi_{1,2}$ implies the oscillations vary along two principle axes. As is well known, the cusp unfolds into two fold caustics, mimicking the roots of the polynomial $t^3 + \xi_2 t + \xi_1$ where three rays/roots coalesce on $\xi_1 = \xi_2 = 0$, and two coalesce on the bifurcation set $4\xi_2^3 = -27\xi_1^2$. We note that the cusp is accompanied by its local Stokes set, which we have extended to $\theta = 0$ by mapping the exact solution found in chapter 36.5, [**?**].

In both cases, the caustics shown in figure **??** are calculated at fixed radius, R. If we allow R to vary it follows that the fold caustic forms a smooth sheet (modulo the cusp kinks) and the cusp forms a cusp rib, both propagating into the nearfield.

While both caustics form the key structural components of the field, there are two additional structures that are important. The first is the Schwarzschild line θ_S, characterised by a double

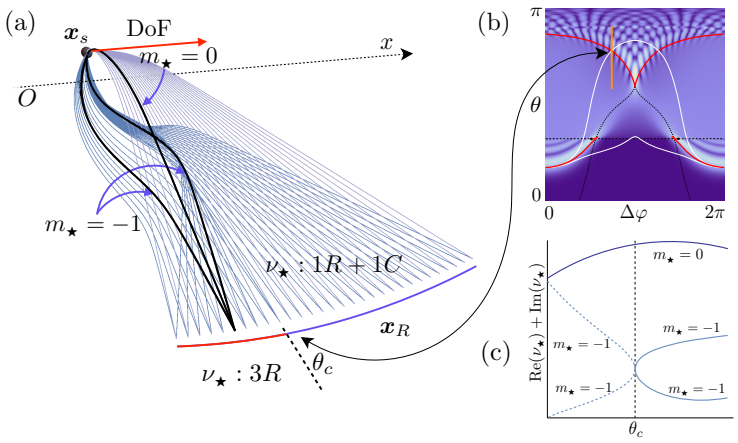

Figure 5: Contributing cusp rays, R, real; C, complex. (a) $\mathrm{Re}(\boldsymbol{x}(\varsigma))$ ray paths for (orange line) cross-section $\Delta\varphi = 3\pi/4\,(135^\circ)$ of $|\mathbb{G}_\omega/\mathscr{G}_\omega|$ shown in (b). Rays labelled with Poisson index, $m_\star$ (**??**, **??**), according to bifurcation diagram (c). DoF, direction of flow; θ_c cusp intersection angle. Red part receiver curve, $\theta > \theta_c$; blue part, $\theta < \theta_c$. Electronic materials attached allow reader to change viewpoint.

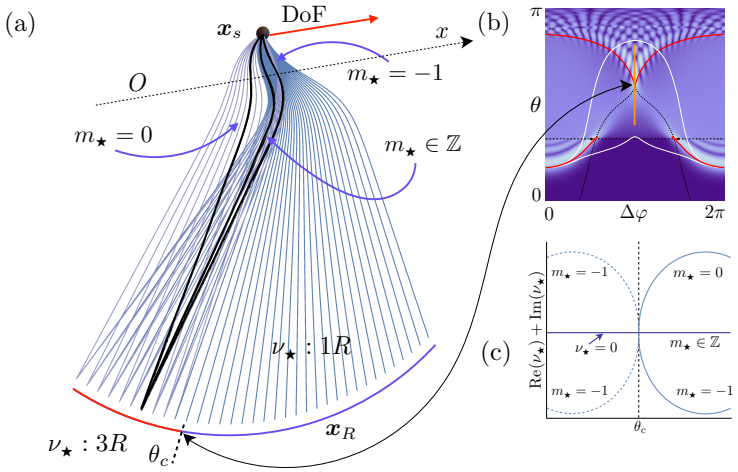

Figure 6: Contributing cusp rays $\mathrm{Re}(\boldsymbol{x}(\varsigma))$ (a), and bifurcation diagram (c), for cross-section $\Delta\varphi = \pi\,(180^\circ)$ of $|\mathbb{G}_\omega/\mathscr{G}_\omega|$ shown in (b). Key as in figure **??**.

turning-point in the radial equation which is independent of $\Delta\varphi$ (see (**??**) and figure **??**). Not only do fold oscillations wash out upon crossing θ_S (see figure **??**), but for the flow studied here the caustic evaporation marks the tangential intersection of the fold with θ_S.

The second structure, the ray delimiter shown by the white line in figure **??**, is not really a structural entity *per se*, but a useful tool for our local analysis in section **??**. This structure delimits the region where the continuation of the ray pair that coalesce at the fold are "indirect". By this we mean that both ray trajectories initially propagate away from the receiver before being turned by the flow (see [**?**] and Powles *et al.* [**?**]). The key to this region, used in section **??**, is that it contains the caustic evaporation points and, as we discover, additional cusps.

In the following sections we shall analyse each of the structures independently before assessing their influence upon the field in both isolated point source cases and as contributors to a source distribution.

4. The cusp and its far-field genesis

We start by analysing the structure of the cusp. Here our point of view concerns the genesis of the cusp structure formed by those rays that propagate out to the far-field as opposed to the analysis of intricate near-field structures that arise from a trapped ray field (see [**?**]). Analysis is aided by use of the Poisson sum formulation of [**?**] shown in appendix **??**, recasting the modal summation (**??**) as $\mathscr{R}_\omega \sim \mathscr{R}_\omega^{(-)} - \mathrm{i}\mathscr{R}_\omega^{(+)}$. This modal rearrangement allows us to consider saddle point expansions of $\mathscr{R}_\omega^{(\pm)}$ in $\nu_\star$, equivalent to rays (Chapman *et al.* [**?**]), so we can write ray contributions as the sum

$$\mathscr{R}_\omega^{(\pm)} \sim \sum_{\nu_\star} \left(r_s Q(r_s|\nu_\star) \frac{\partial \psi}{\partial \nu_\star} \right)^{-1/2} \mathrm{e}^{\mathrm{i}k_0(\alpha_{m_\star}\nu_\star + \zeta(r|\nu_\star) \pm \zeta(r_s|\nu_\star) - R\sin^2\theta)}. \tag{4.1}$$

We then use the equivalence between the saddles, $\nu_\star$, and ray trajectories (see Pierce [**?**]) to label the rays using the Poisson index, $m_\star$. This provides closure to the large θ ray contributions missing from [**?**], and describes the rays' behaviour from an analytical perspective.

The ray trajectories are numerically integrated solutions of the initial value problem in Cartesian coordinates (x, y, z) as shown in [**?**,**?**]

$$\frac{\mathrm{d}\boldsymbol{x}}{\mathrm{d}\tau} = \boldsymbol{T}(\boldsymbol{x}) \cdot \boldsymbol{p} + \boldsymbol{M}(\boldsymbol{x}), \quad \frac{\mathrm{d}\boldsymbol{p}}{\mathrm{d}\tau} = -\frac{1}{2}\nabla_{\boldsymbol{x}} \left(\boldsymbol{p}^\top \boldsymbol{T}(\boldsymbol{x}) \cdot \boldsymbol{p} \right) - \nabla_{\boldsymbol{x}} (\boldsymbol{M}(\boldsymbol{x}) \cdot \boldsymbol{p}), \tag{4.2, 4.3}$$

where $\boldsymbol{x}$ and $\boldsymbol{p}$ are the ray position and slowness vector (or wavefront normal), respectively, both functions of travel time τ with initial conditions $\boldsymbol{x}(0) = \boldsymbol{x}_s$ and $\boldsymbol{p}(0) = \boldsymbol{p}_s$. Additionally

$$\boldsymbol{T}(\boldsymbol{x}) = (\boldsymbol{I} - \boldsymbol{M}(\boldsymbol{x}) \otimes \boldsymbol{M}(\boldsymbol{x})), \quad \boldsymbol{M}(\boldsymbol{x}) = \mathbf{i} M(r), \tag{4.4}$$

where $\boldsymbol{I}$ is the unit matrix, $\otimes$ denotes an outer product and $\nabla_{\boldsymbol{x}}$ the gradient operator in (x, y, z).

As in [**?**,**?**], (**??**, **??**) are recast into a two-point boundary value problem allowing us to cut the singularity structure of the cusp and record the relevant trajectories. As we know from the unfolding of the cusp, we need only cut it in two places to observe two and three ray caustics, the latter which will confirm we really are dealing with a cusp. Cutting the cusp is achieved by parameterising the receiver $\boldsymbol{x}_R$ by θ, with $\Delta\varphi = \mathrm{const.}$ generating cross-sectional slices of $\mathbb{G}_\omega$.

The results of our two-point boundary calculation are shown in figures **??** and **??** with accompanying $\nu_\star$ bifurcation diagram for off-symmetry line and symmetry line cases, respectively. In the first of these figures, we make several observations. The first is that the coalescing ray couple share the same orientation of path about the jet axis, while the third ray takes path encircling the axis in the opposite sense. The choice of orientations is reflected in the Poisson index, $m_\star$, with coalescing rays sharing the same value.

The second observation concerns the qualitative behaviour of the real ray triplet appearing at angles $\theta > \theta_c$, where θ_c is the cusp intersection angle. The majority of these rays, including those that are singular on the cusp, initially propagate in the direction of the flow (see figure **??**) before creeping back against the flow. This counter-intuitive behaviour is one of the reasons the cusp has not been undiscovered until now. Analytically this upstream propagation can be seen as the result of a battle between flow and slowness vector $\boldsymbol{p}$ in (**??**). Initially the flow term $\boldsymbol{M}$ dominates before conceding to the term $\boldsymbol{T} \cdot \boldsymbol{p}$ as the ray propagates. This means that $\boldsymbol{p}$, which maintains a similar value to $\boldsymbol{p}_s$ the initial orientation of the ray trajectory, ultimately prevails.

The final observation relates to the orientation of ray trajectories about the jet axis when the receiver is placed on the symmetry line, as shown in figure **??**. As opposed to the off-axis case there is no preferred route for the coalescing rays: two rays propagate with opposite orientations about the axis, the third propagates through the axis. This discord between real ray trajectories is reflected in Poisson index for $\theta > \theta_c$ (see (c) of figure **??**).

5. Ray vanishing and apparent fold evaporation

(a) A ray vanishes

Having previously considered the cusp we now look at the fold caustic near θ_S. As figure **??** shows, the fold appears to evaporate near to θ_S, where its oscillations also fade away. The field for $\theta < \theta_S$ is supported by two real rays that coalesce at the fold, where for $\theta > \theta_S$ one of these real rays has either vanished, or become complex. A local analysis confirms the latter.

Before we go into detail, we can summarise what is known about the Schwarzschild line. First, as it is a radial equation property, it is independent of $\Delta\varphi$. Secondly, on this line it is known that an indirect saddle, that is a saddle $\nu_\star$ of the integral (setting $m = 0$ in (**??**))

$$\mathscr{R}_\omega^{(+)} \sim \int_{\mathscr{C}^{(+)}} \left(\frac{\mathrm{i}k_0}{2\pi r_s Q(r_s|\nu)} \right)^{1/2} \mathrm{e}^{-\mathrm{i}k_0 P_h(\nu; r_s, \Delta\varphi, \theta)} \, \mathrm{d}\nu, \tag{5.1}$$

where

$$P_h(\nu; r_s, \Delta\varphi, \theta) = -\left(\Delta\varphi\nu + \zeta(r|\nu) + \zeta(r_s|\nu) - R\sin^2\theta \right), \tag{5.2}$$

tends to zero, where according to [**?**] the saddle vanishes. Not only does θ_S represent a locus of second order turning-points as $\nu = \nu_\star \to 0$ in (**??**) (since $\nu = n/k_0$), but ray evaluations of (**??**) erroneously vanish as $\theta \to \theta_S$ according to $O(\nu_\star^{1/2})$ as shown by (**??**).

It can be seen by the ray delimiters in figure **??** that the fold caustic rays are both saddles of (**??**) in the vicinity of the evaporation point, meaning we only need to analyse the integral $\mathscr{R}_\omega^{(+)}$ (and not $\mathscr{R}_\omega^{(-)}$) to work out the rays' controlling structure. As the turning-point used in the radial equation is of the simple type, we set $r_\delta = r_{\delta_1}$ from now on.

(b) Local analysis

In this section we show that the ray solutions about the Schwarzschild line and caustic evaporation point are controlled by the sum of a quadratic polynomial and logarithmic term. This form can be seen as the unfolding of the local form valid on the Schwarzschild line as the receiver is perturbed away from it.

We start by reconsidering the radial equation on the Schwarzschild line noting that its locus is characterised by the saddle $\nu_\star = 0$ and a second order turning-point at $r = 0$ (see figure **??**). The local behaviour of $q^2(r, \theta)$ is given by (**??**, **??**), so we can write the local radial equation as

$$\frac{\mathrm{d}^2 v}{\mathrm{d}r^2} + k_0^2 \left(T_0(\theta) + T_2(\theta) r^2 - \frac{\nu^2}{r^2} \right) v = 0, \tag{5.3}$$

using the scaling $\nu = n/k_0$ of appendix **??**. Now under the ray approximation (**??**) we know that the radial solutions must be evaluated at the saddle point, i.e., $\nu = \nu_\star = 0$ in (**??**), due to the recasting of (**??**) using the Poisson formula. As before, evaluation on the Schwarzschild line gives $Q^2(r|\theta_S) \sim T_2(\theta) r^2$. In this case (**??**) is soluble in terms of Bessel functions of order $\pm 1/4$, (see (**??**)). For example for $v_2(r_s)$ we have

$$v_2(r_s) \sim \sqrt{\frac{\pi r_s}{2}} \mathrm{e}^{-3\pi\mathrm{i}/4} \left[\mathrm{e}^{\pi\mathrm{i}/8} J_{-\frac{1}{4}} \left(k_0 r_s^2 \sqrt{T_2}/2 \right) - \mathrm{e}^{-\pi\mathrm{i}/8} J_{\frac{1}{4}} \left(k_0 r_s^2 \sqrt{T_2}/2 \right) \right], \tag{5.4}$$

where constants are fixed by matching with the WKB integrand found in $\mathscr{R}_\omega^{(+)}$. However, we cannot use this Taylor expansion in $v_1(r)$ as q^2 tends to a constant in the far-field and the above approximation would violate this. The solution is to change the phase reference (i.e., the domains of integration) of $v_{1,2}$ by examining their joint phase contributions to the integrand of $\mathscr{R}_\omega^{(+)}$, which is $\zeta(r_s|\nu) + \zeta(r|\nu)$. We partition these contributions by rewriting the limits of integration as $\int_{r_\delta}^{r_s} + \int_{r_\delta}^{r} = 2\int_{r_\delta}^{r_s} + \int_{r_s}^{r}$, so that we can use the Taylor approximation within the limits $r_\delta < r' < r_s$, and take the out-of-flow approximation, $M(r) \to 0$, for integration over $r_s < r' < r \to +\infty$.

We reflect this change of integration by recasting our radial Green function components as

$$\tilde{v}_1\tilde{v}_2 = v_1(r)v_2(r_s), \tag{5.5}$$

where $\tilde{v}_1$ and $\tilde{v}_2$ contain the phase terms $\tilde{\zeta}_1 = \int_{r_s}^{r} Q(r'|\nu)\mathrm{d}r'$ and $\tilde{\zeta}_2 = 2\int_{r_\delta}^{r_s} Q(r'|\nu)\mathrm{d}r'$, respectively. These new components have WKB expansions

$$\tilde{v}_1 \sim \mathrm{e}^{+\mathrm{i}k_0\tilde{\zeta}_1}, \quad \tilde{v}_2 \sim -\mathrm{i}Q^{-\frac{1}{2}}(r_s|\nu)\mathrm{e}^{+\mathrm{i}k_0\tilde{\zeta}_2}, \tag{5.6}$$

where neglected constants $\gamma_{ij}^{(k)}$ are otherwise cancelled by the Wronskian, $\mathscr{W}$ (see section **??**).

Crucially, the function $\tilde{v}_2$ contains r_s and r_δ interactions only, whereas $\tilde{v}_1$ is independent of r_δ. Under the same Taylor approximations as before we can solve $\tilde{v}_2$ with $\nu = \nu_\star = 0$ in terms of Bessel functions. However, rather than rewriting (**??**) again, we use the special case of the Pearcey function on its symmetry line (see (36.2.19), [**?**]) to give the local radial structure on θ_S as

$$\tilde{v}_1 \sim \mathrm{e}^{+\mathrm{i}k_0(r-r_s)\sin\theta}, \quad \tilde{v}_2 \sim \sqrt{\frac{2^{3/2}}{\pi}}k_0^{-1/4}T_2^{-1/8}\mathrm{e}^{\mathrm{i}k_0 r_s^2\sqrt{T_2}}\mathrm{e}^{-3\pi\mathrm{i}/4}P(0, 2\sqrt{2}k_0^{1/2}T_2^{1/4}r_s). \tag{5.7}$$

The local form (**??**) suggests the strategy we now use to understand the underlying structure of the wavefield. We further our local analysis by including non-zero ν terms in an expansion that unfolds the Schwarzschild line behaviour. Again we use the Taylor expansion (**??**) in $\tilde{\zeta}_2$ and out-of-flow approximation $M \to 0$ in $\tilde{\zeta}_1$, but retain singular term ν^2/r^2. The phase integrals are now

$$\tilde{\zeta}_1 = \int_{r_s}^{r}\sqrt{1-\cos^2\theta - \frac{\nu^2}{r'^2}}\mathrm{d}r',\ r\to+\infty; \quad \tilde{\zeta}_2 = 2\int_{r_\delta}^{r_s}\sqrt{T_0(\theta)+T_2(\theta)r'^2 - \frac{\nu^2}{r'^2}}\,\mathrm{d}r'. \tag{5.8, 5.9}$$

We note that unlike our first approximation of $\tilde{\zeta}_2 \approx 2\int_{r_\delta}^{r_s}\sqrt{T_2(\theta)}r'\,\mathrm{d}r'$ valid on θ_S, where the turning-point is $r_\delta = 0$, the turning-point of (**??**) satisfies the closed form expression

$$r_\delta = \left((\sqrt{T_0^2 + 4\nu^2T_2} - T_0)/2T_2\right)^{1/2}, \tag{5.10}$$

where for consistency (**??**) is the corresponding $r_\delta \in \mathbb{R}^+$ of the four roots that satisfy $Q(r_\delta|\nu) = 0$ under the truncated Taylor regime.

With both phases (**??**, **??**) integrable, we expand their solutions sequentially using the small parameters $T_0, \nu \to 0$, as $\theta \to \theta_S$. We perform the expansion in T_0 to first order and then expand in ν up to powers of ν^4, in what is a post-paraxial approximation (see Ring *et al.* [**?**]) and one motivated by the Pearcey function in the radial solution (**??**).

Once expanded the phase of P_h of (**??**) can be written

$$P_h \sim c_4\nu^4 + c_2\nu^2 + c_1\nu + c_0\ln(\nu) + f(r_s, \theta, M_J), \tag{5.11}$$

where

$$c_0 = \frac{T_0}{2\sqrt{T_2}}, \quad c_1 = \left(\frac{\pi}{2} - \Delta\varphi\right),$$
$$c_2 = \left(\frac{T_0}{8r_s^4T_2^{3/2}} + \frac{1}{2r_s\sqrt{1-\kappa_\star^2}} - \frac{1}{2r_s^2\sqrt{T_2}}\right), \quad c_4 = \left(\frac{1}{24r_s^3(1-\kappa_\star^2)^{3/2}} + \frac{9T_0 - 8r_s^2T_2^2}{192r_s^8T_2^{5/2}}\right), \tag{5.12}$$

with $f(r_s, \theta, M_J)$ collecting terms independent of ν, and $\kappa_\star = -\cos\theta$.

Retaining only those terms that affect the dynamics of the local form (i.e., only functions of ν) leads us to discard $f(r_s, \theta, M_J)$ from (**??**). We can now define a new codimension-3 integral form based on the expansion (**??**), which takes on a similar guise to those of catastrophe theory once rescaled to leave ν^4 independent of receiver variables. Modulo the constants due to the Jacobian

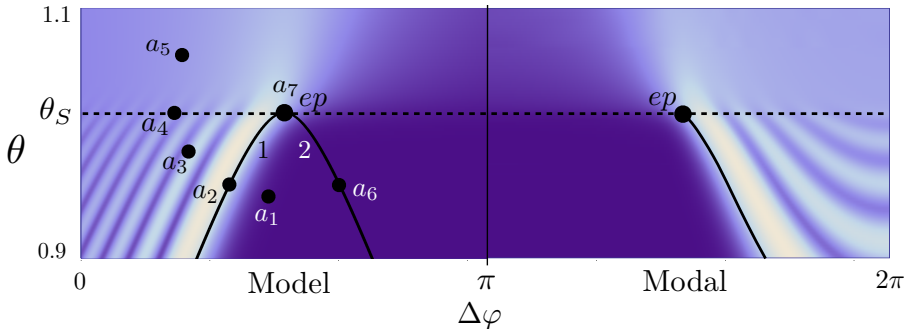

Figure 7: Modelled ($0 \leq \Delta\varphi < \pi$) and modal ($\pi \leq \Delta\varphi \leq 2\pi$) fields for $St = 17.7$, $k_0 = 100$, $r_s = 0.45$. Caustics (black solid line) leading to evaporation points, *ep*. L.H.S. folds labelled 1 & 2. Dashed line, Schwarzschild line, θ_S. Control points $\boldsymbol{a}$ (black) for saddle analysis.

and logarithm of this rescaling, and the slow function $(\mathrm{i}/2\pi r_s Q(r_s|\nu))^{1/2}$ of (**??**), we have

$$I(\bar{\boldsymbol{c}}) \equiv k_0^{1/2} \int_0^{+\infty} \mathrm{e}^{-\mathrm{i}k_0\left(\nu^4 + \bar{c}_2\nu^2 + \bar{c}_1\nu + \bar{c}_0 \ln(\nu)\right)} \,\mathrm{d}\nu, \quad \bar{\boldsymbol{c}} = (\bar{c}_0, \bar{c}_1, \bar{c}_2), \tag{5.13}$$

where the coefficients $\bar{c}_2 \equiv c_2/\sqrt{c_4}$, $\bar{c}_1 \equiv c_1/c_4^{1/4}$, $\bar{c}_0 \equiv c_0$, are allowed to take on complex values when $c_i \in \mathbb{R}$, $i = 1, \ldots, 4$. The effective codimension-3 nature of $\bar{\boldsymbol{c}}$ and (**??**) is also reflected in the controlling parameters $\Delta\varphi, r_s, \theta$ for a constant Mach no., $M_J = \mathrm{const}$.

The new integral form allows us to make a straightforward numerical comparison straight away. Initially we choose $r_s = 0.45$ to ensure the underlying approximation (**??**) makes a decent estimate of the phases ζ, where the structure of $r_s = 0.75$, pertinent to figure **??**, is considered below. Figure **??** shows both modelled (**??**) and modal (**??**) fields for $r_s = 0.45$ with caustic and Schwarzschild structures. In the case of the modelled field we note that the caustics are centred about $\Delta\varphi = \pi/2$, the zero of $\bar{c}_1$, and the evaporation point of I.

The first comparison we make is upon the qualitative features of the field. As expected from local expansion about $\nu = 0$, the best match is found in the vicinity of the evaporation point where both fold saddles tend to 0. The agreement is notably broken by the increasing misalignment of the model's oscillations with increasing lateral distance from $\Delta\varphi = \pi/2$. There are two reasons for this: first, the local mapping becomes increasingly poor as the saddles move away from $\nu = 0$; second, the function I is only the transitional solution about the evaporation point and a full mapping would include derivatives of I with respect to $\bar{\boldsymbol{c}}$ (see [**?**] and Bleistein [**?**]).

The second comparison we make is of the structural behaviour. We note that the model predicts a continuous branch of caustics, caustics 1 and 2 in figure **??**, whereas only caustic 1 can be determined in the modal solution using the methods of [**?**,**?**]. As we show below, caustic 2 is resolved by examining the Riemann sheet structure of I. The curvature of caustic 1 and that of the modal field match near to the evaporation points, while the Schwarzschild lines match exactly. Note that for this source radius neither field contains the cusp kinks of figure **??**. We now go onto explain when and why they occur.

The appearance of caustics exhibited by figure **??** can be understood by examining the underlying singularity structure of I. This is given in $\bar{\boldsymbol{c}}$ by solving $\partial P_h/\partial\nu = \partial^2 P_h/\partial\nu^2 = 0$. These conditions are equivalent to two fourth-order polynomials, and as we show in Stone *et al.* [**?**], yields a singularity structure that is the swallowtail catastrophe (chapter 36.4, [**?**]) albeit with complex coefficients. Here the caustic is given implicitly by

$$128\bar{c}_0^3 - 64\bar{c}_0^2\bar{c}_2^2 + 36\bar{c}_0\bar{c}_1^2\bar{c}_2 + 8\bar{c}_0\bar{c}_2^4 - \tfrac{27}{8}\bar{c}_1^4 - \bar{c}_1^2\bar{c}_2^3 = 0, \tag{5.14}$$

so that despite the $\ln(\nu)$ of (**??**) suggesting non-canonical behaviour, the overall swallowtail structure is both *canonical* and *structurally stable*. This may be confirmed by a formal coordinate transformation, [**?**].

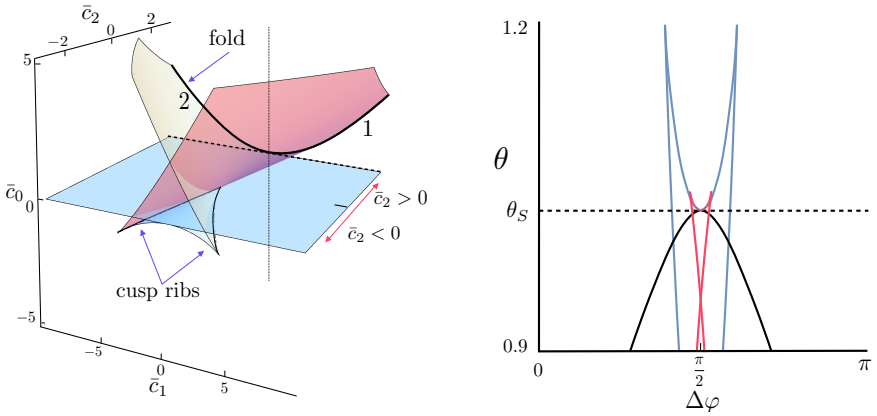

(a) (b)

Figure 8: Swallowtail singularity set in $\bar{\boldsymbol{c}}$, (a) and intersections in the $(\Delta\varphi, \theta)$ plane, (b). (a) solid line shows how caustics 1 & 2 of figure **??** arise. Dashed line, Schwarzschild line on plane $\bar{c}_0 = 0$. Cusp ribs exist for $\bar{c}_2 < 0$. (b) resulting caustics/Schwarzschild lines for various source radii. Black line, $r_s = 0.45$ (as in figure **??**); red line, $r_s = 0.75$; blue line, $r_s = 0.9$; black dashed line, θ_S.

The singularity set (**??**) is shown in figure **??** with equivalent cross section for $r_s = 0.45$. The swallowtail structure shows how the fold caustics, 1 & 2, of the model appear and how they merge with the Schwarzschild plane $\bar{c}_0 = 0$ equivalent to θ_S. An important feature of figure **??** is the existence of cusp ribs for $\bar{c}_2 < 0$. For certain source positions cusps do appear in $\mathbb{G}_\omega$ as shown by figure **??** for swallowtail cross-sections at $r_s = 0.75, 0.9$, in the $(\Delta\varphi, \theta)$ plane. This leads us to conclude that the cusp-like kinks near to the evaporation points of figure **??** really are cusps. A notable prediction that is true even though $r_s \geq 0.75$ is perhaps outside the range of validity of the original Taylor expansion (**??**).

Even though the model field has a symmetric caustic structure about the evaporation point, this is clearly not reflected in the field amplitude as would be by the swallowtail catastrophe (chapter 36.3, [**?**]). The intricacies of the model field and its implications for $\mathbb{G}_\omega$ become clear if we track the saddle expansion of I as $k_0 \to +\infty$ about the evaporation point $(\pi/2, \theta_S)$. We do this for $r_s = 0.45$, though the ray mechanisms behind the Schwarzschild line and evaporation point are the same for all source radii considered in this paper. We examine further the case $r_s = 0.75$ in [**?**].

Using the control points $\boldsymbol{a} = \{a_1, \ldots, a_7\}$ of figure **??**, we determine which of the saddles contribute to the field using the method of steepest descents (SD) [**?**]. For convenience we unfold the logarithmic singularities of (**??**) by transforming $\nu = \mathrm{e}^w$, where the saddles $w_\star$ satisfy the saddle condition

$$\partial P_h/\partial w_\star = 4\mathrm{e}^{4w_\star} + 2\bar{c}_2\mathrm{e}^{2w_\star} + \bar{c}_1\mathrm{e}^{w_\star} + \bar{c}_0 = 0. \tag{5.15}$$

This transformation returns the primary saddles $w_\star$ and an infinite number of images, i.e., $w_{\star,k} = w_\star + 2\pi\mathrm{i}k$, $k = 0, \pm1, \pm2, \ldots$. Note that $k = 0$ returns the primary saddle. The SD contour then ascends from the valley at complex infinity with orientation chosen in order to assure convergence. We label the saddles (ℓ, k) where ℓ labels one of the four primary saddles, with k as before. The contributing saddles are then mapped back to $\nu_\star$ and I is evaluated using the ray sum

$$I \sim \sum_{\nu_\star} \mathrm{e}^{\pi\mathrm{i}/4}\mathrm{e}^{-\mathrm{i}k_0 P_h(\nu_\star;\bar{\boldsymbol{c}})}\sqrt{2\pi/\partial^2 P_h/\partial\nu_\star^2}, \tag{5.16}$$

where it can be shown that the ray amplitude vanishes as $(2\pi\nu_\star/\bar{c}_1)^{1/2}$ when $\nu_\star \to 0$ as $\theta \to \theta_S$, in agreement with the order of $\nu_\star$ found in the vanishing ray amplitude of $\mathscr{R}_\omega^{(+)}$.

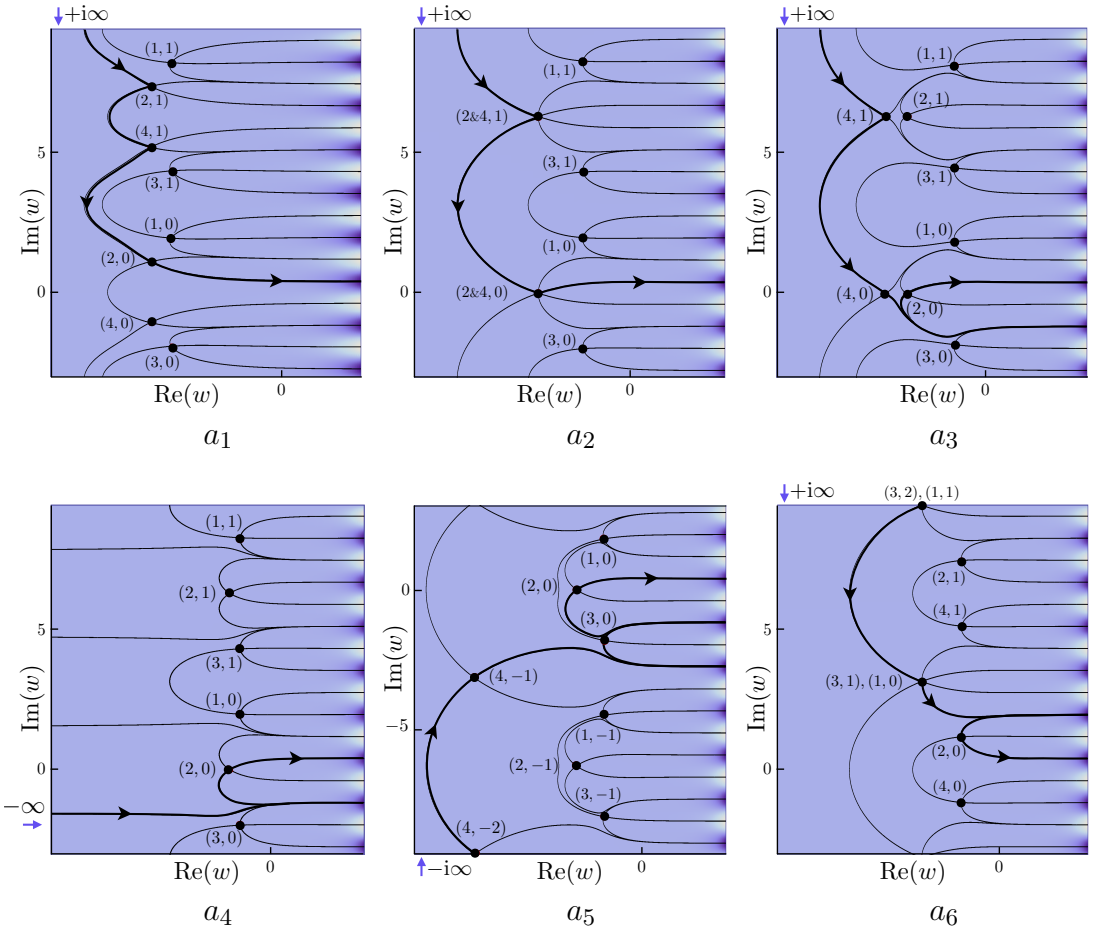

Figure 9: SD paths (thick black line) for control points $\boldsymbol{a} = \{a_1, \ldots, a_6\}$. Purple arrow shows origin of contour from complex infinity; black arrows, SD path direction. Saddles (black points) labelled according to (ℓ, k) where ℓ labels the primary saddle and k the image number.

Figure **??** shows the SD paths for control points $\{a_1, \ldots, a_6\}$. Starting with a_1 in figure **??**, we note that the receiver, located in the cone of silence, picks up a complex ray $(2, 0)$ and an infinite number of exponentially small images of itself and of its conjugate $(4, 0)$. The conjugate pair then coalesce at a_2, coincident with caustic 1 (the fold, θ_f, see figure **??**) as do all their image pairs. As the receiver moves from a_2 to a_3 the complex rays emerge post coalescence with $(2, 0), (4, 0)$ a real ray pair. So far, so canonical.

Control point a_4 (see figure **??**) sees all saddles $(4, k)$, $\forall k$, move off and cluster at infinity. This is of course equivalent to $\nu_\star \to 0$ at θ_S. Moving to a_5 then sees the return of $(4, k)$ to the finite plane, making exponentially small contributions in the presence of $(2, 0)$,

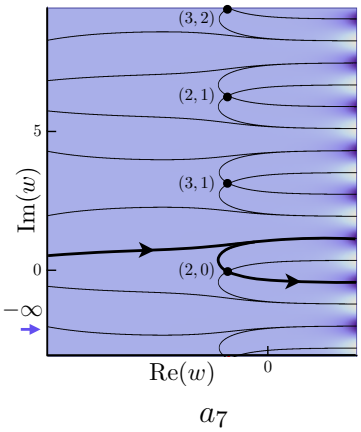

Figure 10: SD paths at the evaporation point. Key as in figure **??**.

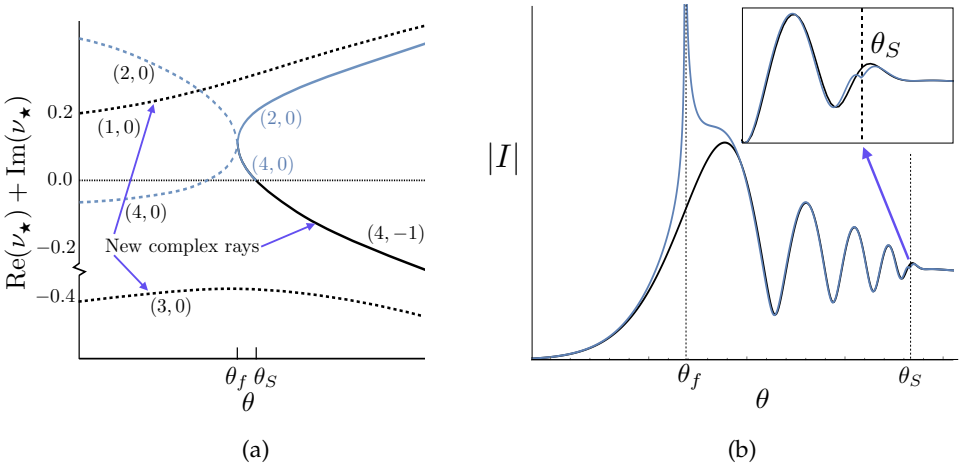

Figure 11: Saddle bifurcations and amplitude evaluation for $\Delta\varphi = 1.3\,(74.5^\circ)$, $St = 177$, $k_0 = 1000$, $r_s = 0.45$. (a) Solid line, real rays; dashed line, complex. Blue line, known branches; black line, new. (b) Black line, $|I|$, (**??**); blue line, ray approximation, (**??**). Inset shows closeup of field about θ_S. θ_f, intercept of fold caustic 1.

which remains real. Note that going from a_4 to a_5 the ray expansion has undergone a Stokes phenomenon picking up exponentially small ray contribution $(3, 0)$.

Traversing around the evaporation point to a_6 lying on caustic 2, the ray expansion again diverges. This time the caustic involves exponentially small rays $(3, \ell + 1), (1, \ell), \ell \geq 0$, which lie on the branch cut of I in the ν-plane (which we take from $(-\infty, 0]$ along the real axis). This is the key to the apparent symmetry breaking properties of I. While the caustic structure is that of the swallowtail, half of this structure pertains to caustics of exponentially damped rays. This caustic would appear in $\mathbb{G}_\omega$ if we had tracked rays onto different Riemann sheets using [**?**]. Hence we arrive at a seemingly paradoxical result that exponentially accurate approximations here lead to an additional caustic divergence whereas a leading order ray approximation does not!

We can examine the evaporation point using a_7 with SD paths shown in figure **??**. Whereas ordinarily crossing θ_S one ray and its images make excursions to infinity, the evaporation point sees two rays, $(1, 0)$ and $(4, 0)$, coalesce while making the same excursions. This results in an otherwise canonical caustic being damped at infinity in the presence of real ray $(2, 0)$.

We can sum ray contributions in $\nu_\star$ using figure **??** for $\Delta\varphi = 1.3$, extending the bifurcation diagram of [**?**]. Recording the new complex branches, e.g., $(4, -1)$ the dominant complex ray for $\theta > \theta_S$, we plot the ray field of I in figure **??**. This figure shows how the rays erroneously predict a kink at θ_S due vanishing amplitude, where the uniform correction is I itself.

While I models the modal field locally about the evaporation point and confirms a swallowtail structure, the number of additional rays present in the upstream region means that $\mathbb{G}_\omega$ is embedded in a hierarchy of more complicate structures (e.g., D_6^+, see [**?**]).

6. Cuspoid magnitude and energy analysis

Now we have determined fully the controlling structures of the Green function we are now in a position to examine the relative importance of each. The first comparison we make is a direct amplitude and energy calculation. In both cases we consider the point source solution.

The aim of this comparison is to identify the largest contributions of the field as a function of $\Delta\varphi$. As is well known, the uniform asymptotic field about a canonical caustic is greatest, not on the caustic, but in the region just behind it. In light of this, figure **??** shows the modal field,

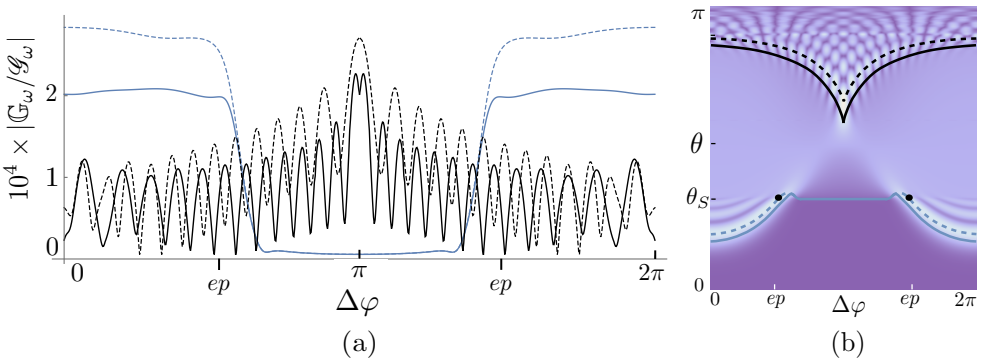

Figure 12: On caustic and maximum value evaluations with colour-coded corresponding paths in $(\Delta\varphi, \theta)$. Black line, on cusp; black dashed line, off cusp; blue line, on swallowtail; blue dashed line, off swallowtail; ep, evaporation points. (a) $10^4 \times |\mathbb{G}_\omega/\mathscr{G}_\omega|$ of (**??**) with $St = 5$, $k_0 = 28.27$, $r_s = 0.75$, evaluated on paths shown in (b) with black points denoting evaporation points.

$|\mathbb{G}_\omega/\mathscr{G}_\omega|$, on four curves: two directly following the path of the caustics (on caustic) and two following the locus of the maximum value of the field in the vicinity of the caustics (off caustic). In order to join the swallowtail evaluations either side of $\Delta\varphi = \pi$, we traverse the Schwarzschild line.

It can be seen that while the swallowtail cross-sections are larger for the most part in $\Delta\varphi$, the maximum values associated with each caustic are commensurate, and though the cusp drops to half the value of the fold away from the maximum, it has a larger distribution in $\Delta\varphi$. This suggests that we should take into account the distribution of the caustics and their attendant diffraction wavefield, not just their maximum values. A suitable way of doing this is using an energy analysis: integrating the energy flow at constant radius R over a representative region containing the caustic maximum values.

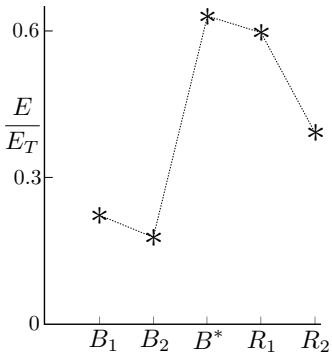

Figure 13: Normalised energy evaluations domains: B_i, B^*, and R_i, $i = 1, 2$.

The energy of the Green function is proportional to the amplitude squared, so we will consider normalised (by $|\mathscr{G}_\omega|^2$ which provides surface element R^2) surface integrals of the form

$$E = \int_D \left| \frac{\mathbb{G}_\omega}{\mathscr{G}_\omega} \right|^2 \sin\theta \, \mathrm{d}\theta \, \mathrm{d}\Delta\varphi, \tag{6.1}$$

where D is the region of integration in $(\Delta\varphi, \theta)$, and gives the total energy, E_T, when $D = [0, 2\pi) \times [0, \pi)$. In the following we use for D: disk domains $B_i = \{\boldsymbol{p} \in (\Delta\varphi, \theta) : |\boldsymbol{p} - \boldsymbol{q}| \leq 1\}$ about the evaporation point $(i = 1, \boldsymbol{q} = (\pi/2, \theta_S))$, and cusp point $(i = 2, \boldsymbol{q} = (\pi, \theta_c))$; and rectangular domains $R_1 = [0, 2\pi) \times [0, \pi/2)$, $R_2 = [0, 2\pi) \times [\pi/2, \pi)$, for downstream and upstream fields, respectively.

The results of this study are shown in figure **??**, where we have included energy due to $B^* = B_1 \cup B_2$, which is equal to the energy sum of disks about both evaporation points (counting B_1 twice) and the cusp point. These results show that the energy contained in equivalent area disks about the cusp and the evaporation point is of similar magnitude, and that the combination

of these energies using B^* accounts for over half the field energy. This is more than that of both the upstream and downstream regions individually.

The relevance of energy contained in B_i, is due to the beaming of the caustics towards observers in aircraft noise evaluations. For instance, when the source is placed at $\varphi_s = \pi/2$, B_2 is a useful measure of the cusp's impact at flyover certification points (see Smith [**?**]), despite the cusp rib in 3D providing a more complicated acoustic signature at a microphone compared with analysis at $R = \text{const}$. As we show in section **??**, distributions of sources lead to distributed caustics, meaning they are relevant at all microphone positions, particularly lateral and flyover positions where the jet engine is at, or is near to, its maximum power setting.

7. Aggregate effect of singularities

To test the persistence of the caustic structures, in this section we consider the effect of multiple off-axis sources upon the catastrophe fields analysed above (using the same flow profile). We first consider the combination of discrete source distributions as one might expect in engineering implementations of acoustic analogies to non-separable flows, [**?**]. In such circumstances the convolution of the Green function with a source distribution is replaced by a series of weighted point source solutions of the fields similar to that shown in figure **??**. We then move on to variations of continuum ring source models popular in aeroacoustics, as used in [**?**] and [**?**].

(a) Multiple point sources

The effect of multiple point sources on the field can be examined easily if they lie on the same source radius due to the separable nature of the Green function (**??**). A sum of N_s Green functions with equal source weighting is given by

$$\frac{1}{\mathscr{G}_\omega}\sum_{m=1}^{N_s}\mathbb{G}_\omega(\varphi|\varphi_{s_m}) = \frac{\mathrm{i}\mathrm{e}^{-\mathrm{i}k_0 R\sin^2\theta}}{\bar{c}_\infty k_0 \Phi_s^2}\sum_{n=-\infty}^{+\infty}\left(\frac{2}{k_0}\frac{\sqrt{-\eta_n^{(1)}(r_s)}}{r_s Q_n(r_s)}\right)^{1/2}\mathrm{Ai}\left(\eta_n^{(1)}(r_s)\right)\mathrm{e}^{\mathrm{i}k_0\zeta_n(r)}\times \\ \mathrm{e}^{\mathrm{i}n\Delta\varphi}\left[1+\mathrm{e}^{\mathrm{i}k_0\Delta\varphi_{12}}+\ldots+\mathrm{e}^{\mathrm{i}k_0\Delta\varphi_{1m}}+\ldots+\mathrm{e}^{\mathrm{i}k_0\Delta\varphi_{1N_s}}\right], \tag{7.1}$$

where the single turning-point solution to (**??**) is used and in this instance $\Delta\varphi = \varphi - \varphi_{s_1}$, $\Delta\varphi_{1m} = \varphi_{s_1} - \varphi_{s_m}$ and φ_{s_m} is the mth of N_s source azimuths as illustrated in figure **??**, (i).

The aggregate fields for $N_s = 2, 3$ with radius $r_s = 0.75$ are shown in figure **??**. Unsurprisingly, in the cases where these sources are symmetrically placed, i.e., figures **??** and **??**, the fields are periodic in $\Delta\varphi$. Conversely, asymmetric source positioning in figures **??** and **??** leads to an asymmetric field which is somewhat disordered. In each case the field is complicated by the overlapping diffraction patterns, effectively leading to a completely decorated field. One notable consequence of this distribution is the apparent reduction in cusp intensity. We might then ask if continuing the process of adding points sources in the manner of (**??**) *ad infinitum* ($N_s \to +\infty$) might see the cusp disappear completely. This limiting case, known as a ring source, would conclude the impact of repeated overlapping of each interference pattern.

(b) Ring sources

Ring sources are frequently used in aeroacoustics as a model simplification (see for e.g., [**?**], Khavaran *et al.* [**?**]). They reflect the turbulence physics by concentrating the source in the shear layer of the jet. We use the correlation integral setting of [**?**] to arrive at our ring-source directivity

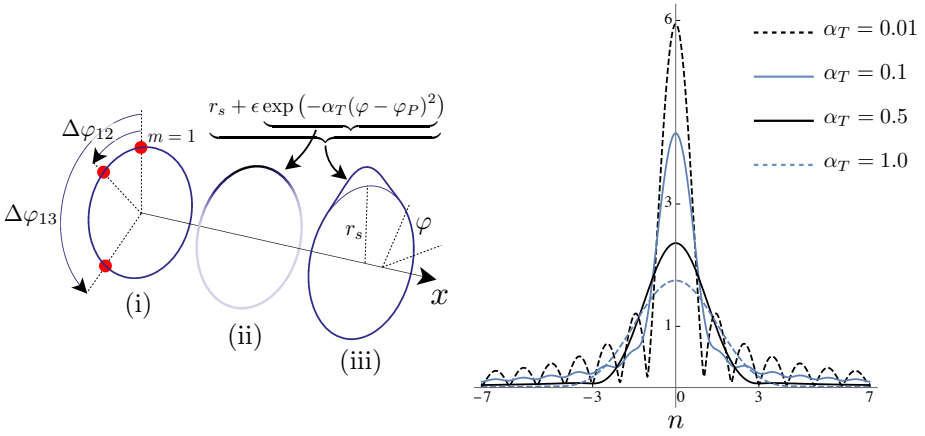

(a) (b) $|\mathscr{Y}(\pi; n, \pi/2, \alpha_T)| : \alpha_T \in (0.01, 0.1, 0.5, 1)$

Figure 14: (a) Source models: (i) Relative spacing between three point sources when $\Delta\varphi_{1m} < 0$, (ii) weighted ring-source, (iii) perturbed ring-source. (b) $|\mathscr{Y}|$ as a function of n and α_T.

function $\mathscr{D}_\omega$. It can be shown from [**?**] that the acoustic intensity in the far-field is written as

$$\begin{aligned} I_\omega &= \frac{1}{\bar{\rho}_\infty \bar{c}_\infty} \int_{V''} \int_{V'} \mathscr{A}_i^* \mathbb{G}_\omega^*(\boldsymbol{x}_R|\boldsymbol{x}_s') \mathscr{A}_j \mathbb{G}_\omega(\boldsymbol{x}_R + \boldsymbol{\eta}|\boldsymbol{x}_s') \hat{s}_{ij}(\boldsymbol{x}_s', \boldsymbol{\eta}, k_0)\, \mathrm{d}^3\boldsymbol{x}_s'\, \mathrm{d}^3\boldsymbol{\eta} \\ &= \frac{|\mathscr{G}_\omega|^2}{\bar{\rho}_\infty \bar{c}_\infty} \int_{V''} \mathscr{D}_\omega(\boldsymbol{\eta}; \boldsymbol{x}_R, k_0)\, \mathrm{d}^3\boldsymbol{\eta}, \end{aligned} \tag{7.2}$$

where V', V'' are integrations over real space, $\bar{\rho}$ is the ambient density, $*$ denotes a complex conjugate, and $\hat{s}_{ij}$ is the Fourier transform in time of the source correlation. The factors $\mathscr{A}_i$ are algebraic and are used to relate $\mathbb{G}_\omega$ to pressure Green functions. The variables $\boldsymbol{\eta}$ are separation coordinates, that is the vector displacement between two source points, $\boldsymbol{\eta} = \boldsymbol{x}_s'' - \boldsymbol{x}_s'$, say.

The ring source model proceeds from (**??**) by taking the source correlation as

$$\hat{s}_{ij} = M_{ij}(\boldsymbol{x}_{\perp_s}', \omega)\delta(\boldsymbol{\eta})\delta(x_s' - x_s). \tag{7.3}$$

Here M_{ij} are source position terms so that $\mathscr{D}_\omega$ depends on the transverse coordinates $\boldsymbol{x}_{\perp_s}' = (y_s', z_s')$, and $\delta(x_s' - x_s)$ reflects the the far-field and x-independent result of the source distribution. The correlation effects are reflected in $\delta(\boldsymbol{\eta})$, which exhibits zero correlation between any two source points that are not coincident. This can be seen as the limit of Gaussian source models used in jet noise (see Morris & Farassat [**?**], Self [**?**]). We make one further simplification, and that is we limit ourselves to just one component of the inner product of the integrand in (**??**), i.e., we set $\mathscr{A}_i = 1$ and take $M_{ij} = M(\boldsymbol{x}_{\perp_s}')$, $\forall i, j$. This makes the source independent of frequency. We claim that the conclusions we draw upon the impact of singularities upon $\mathscr{D}_\omega$ is not undermined by these simplifications.

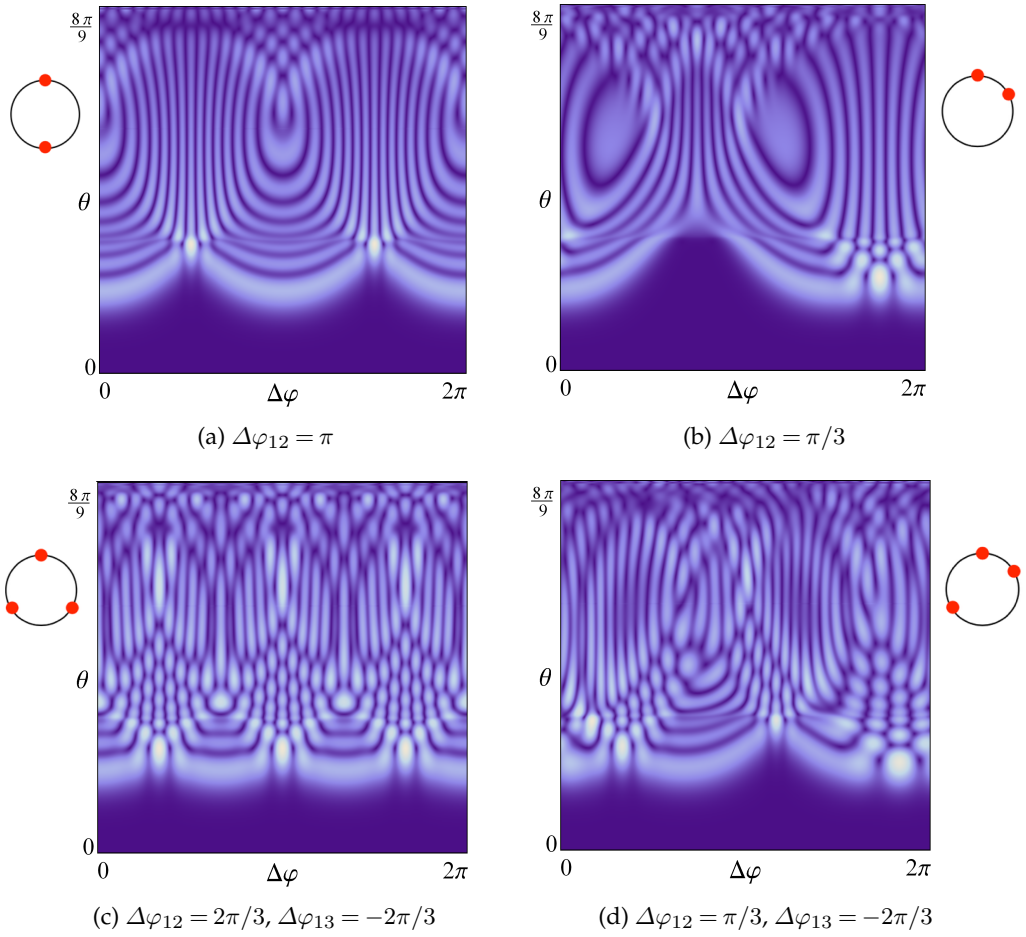

(a) $\Delta\varphi_{12} = \pi$ (b) $\Delta\varphi_{12} = \pi/3$

(c) $\Delta\varphi_{12} = 2\pi/3$, $\Delta\varphi_{13} = -2\pi/3$ (d) $\Delta\varphi_{12} = \pi/3$, $\Delta\varphi_{13} = -2\pi/3$

Figure 15: Field magnitude due to multiple point sources, the magnitude of the LHS of (**??**) plotted as a function of $(\Delta\varphi, \theta)$ with $St = 5$, $k_0 = 28.27$, $r_s = 0.75$. (a, b) Two sources, (c, d) three sources. (a, c) symmetric fields, (b, d) asymmetric fields. Relative azimuthal source positions (red marker). Here $\Delta\varphi = \varphi - \varphi_{s_1}$.

(i) Symmetric ring source

We start by examining a perfectly symmetric ring source. Taking $M(\boldsymbol{x}'_{\perp_s}) = \delta(r'_s - r_s)/r'_s$ we have

$$\begin{aligned}\mathscr{D}_\omega &\sim \frac{1}{|\mathscr{G}_\omega|^2}\int_{-\pi}^{\pi}\int_0^{+\infty} \mathbb{G}^*_\omega(\boldsymbol{x}_R|\boldsymbol{x}'_s)\mathbb{G}_\omega(\boldsymbol{x}_R|\boldsymbol{x}'_s)\frac{\delta(r'_s - r_s)}{r'_s}\, r'_s \mathrm{d}r'_s \mathrm{d}\varphi'_s \\ &= \frac{4\pi}{\bar{c}_\infty^2 k_0^3 \Phi_s^4}\sum_{n=-\infty}^{+\infty}\left(\frac{\sqrt{-\eta_n^{(1)}(r_s)}}{r_s Q_n(r_s)}\right)\mathrm{Ai}^2\left(\eta_n^{(1)}(r_s)\right),\end{aligned} \tag{7.4}$$

since $\int_{-\pi}^{\pi} \mathrm{e}^{\mathrm{i}(m-n)\varphi'_s}\,\mathrm{d}\varphi'_s = 2\pi\delta_{nm}$ (here δ_{nm} is the Kronecker delta). This result equals that of [**?**] and is shown in figure **??**. Not only is it invariant in $\Delta\varphi$, but also exhibits the effects of repeatedly overlapping the cusp and swallowtail caustics giving a constant boundary to the cone of silence and completely washing out the cusp. The latter observation answers the question posed in section **????**, as the cusp effects are eliminated in the $N_s \to +\infty$ limit.

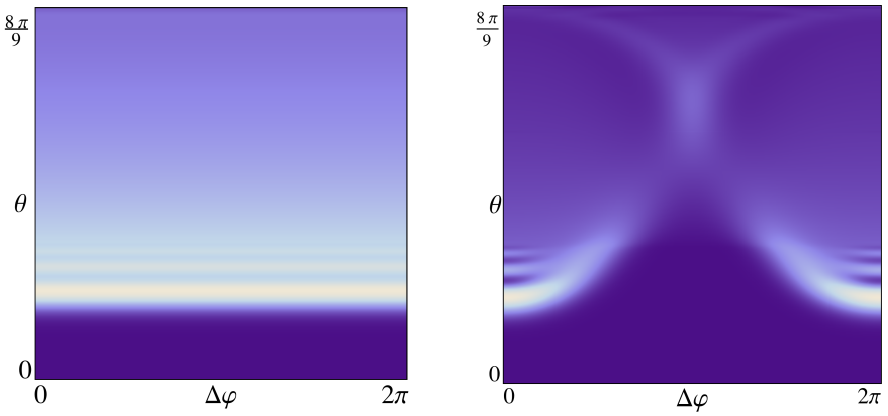

(a) Ring source (b) $\varphi_P = \pi/2$, $\alpha_T = 5$

Figure 16: Field magnitude $|\mathscr{D}_\omega|$ plotted as a function of $(\Delta\varphi, \theta)$ due to (a) symmetric ring source (**??**) and (b) weighted ring source (**??**). Here $\Delta\varphi = \varphi - \varphi_P$ and parameters $St = 5$, $k_0 = 28.27$, $r_s = 0.75$, were used.

(ii) Weighted ring source

The washing out of the cusp shows that perfect symmetry of the ring source eliminates any asymmetry present in the Green function. However, it remains to be seen how the cusp impacts the field if there are small perturbations to this symmetry. In this section we consider perturbations to the ring source weight.

The weighted source uses source correlation of the form $M(\boldsymbol{x}'_{\perp_s}) = h(\varphi'_s; \varphi_P, \alpha_T)\delta(r'_s - r_s)/r'_s$ allowing for the presence of azimuthal variability and its tuning through parameters φ_P and α_T. The former centres the asymmetry, while the latter concentrates it. This results in an integral of the form

$$\begin{aligned}\mathscr{D}_\omega &= \frac{1}{|\mathscr{G}_\omega|^2}\int_{-\pi}^{\pi}\int_0^{+\infty} \mathbb{G}^*_\omega(\boldsymbol{x}_R|\boldsymbol{x}'_s)\mathbb{G}_\omega(\boldsymbol{x}_R|\boldsymbol{x}'_s)h(\varphi'_s;\varphi_P,\alpha_T)\frac{\delta(r'_s - r_s)}{r'_s}\, r'_s \mathrm{d}r'_s \mathrm{d}\varphi'_s \\ &= \frac{1}{|\mathscr{G}_\omega|^2}\int_{-\pi}^{\pi} \mathbb{G}^*_\omega(\boldsymbol{x}_R|r_s,\varphi'_s)\mathbb{G}_\omega(\boldsymbol{x}_R|r_s,\varphi'_s)h(\varphi'_s;\varphi_P,\alpha_T)\,\mathrm{d}\varphi'_s.\end{aligned} \tag{7.5}$$

Choosing a Gaussian form for the weight, i.e., $h(\varphi'_s; \varphi_P, \alpha_T) = \exp(-\alpha_T(\varphi'_s - \varphi_P)^2)$ allows us to find the solution of (**??**) in terms of error functions (see figure **??** (ii) for example of weighting). We then find the azimuthal component is given by

$$\begin{aligned}&\mathscr{Y}(\varphi; n, \varphi_P, \alpha_T) = \int_{-\pi}^{\pi} \mathrm{e}^{\mathrm{i}n(\varphi-\varphi'_s)-\alpha_T(\varphi'_s-\varphi_P)^2}\,\mathrm{d}\varphi'_s = \\ &\frac{\sqrt{\pi}}{2\sqrt{\alpha_T}}\mathrm{e}^{-\frac{n(n+4\mathrm{i}\alpha_T(\varphi_P-\varphi))}{4\alpha_T}}\left[\mathrm{erf}\left(\frac{2\alpha_T(\pi-\varphi_P)+\mathrm{i}n}{2\sqrt{\alpha_T}}\right) - \mathrm{erf}\left(\frac{-2\alpha_T(\varphi_P+\pi)+\mathrm{i}n}{2\sqrt{\alpha_T}}\right)\right].\end{aligned} \tag{7.6}$$

An example of $|\mathscr{Y}|$ is shown in figure **??** for various α_T. The effect of increasing asymmetry, i.e., increasing α_T, affects $|\mathscr{Y}|$ by coupling more modes together with uniform weight near to $n = 0$. Conversely $\alpha_T \to 0$ allows $\mathscr{Y}$ to act as a delta function limit sequence thereby facilitating

uncoupling. It is straightforward to show that Gaussian weight leads to the expression

$$\mathscr{D}_\omega \sim \frac{2}{\bar{c}_\infty^2 k_0^3 \Phi_s^4} \times \sum_{n=-\infty}^{+\infty} \sum_{m=-\infty}^{+\infty} \left(\frac{\sqrt[4]{-\eta_n^{(1)}(r_s)}}{\sqrt{r_s Q_n(r_s)}} \right)^* \left(\frac{\sqrt[4]{-\eta_m^{(1)}(r_s)}}{\sqrt{r_s Q_m(r_s)}} \right) \mathrm{Ai}\left(\eta_n^{(1)}(r_s)\right) \mathrm{Ai}\left(\eta_m^{(1)}(r_s)\right) \times \mathrm{e}^{\mathrm{i}k_0(\zeta_m(r_s)-\zeta_n(r_s))} \mathscr{Y}(\varphi; m\text{-}n, \varphi_P, \alpha_T). \tag{7.7}$$

Equation (**??**) is computed for $\varphi_P = \pi/2$ and $\alpha_T = 5$ as shown in figure **??**. Representing quite a large deviation from the symmetric ring source field, figure **??** draws a stark comparison with symmetric field of figure **??**. Not only do we see the re-emergence of the cusp upstream, but the total field resembles a Green function with smoothed diffraction patterns.

(iii) Perturbed ring source

In the case of an asymmetric source position the argument of the delta function can be adapted. The resulting integrals, however, are more cumbersome than before. Some progress can be made if a perturbed ring source is considered. This permits the construction of a perturbation expansion in a small parameter, $\epsilon \ll 1$, say, as shown in figure **??**, (iii). As a function of ϵ the delta function then expands as

$$\delta(r_s' - g(\varphi_s'; r_s, \varphi_P, \epsilon)) = \delta(r_s' - g(\varphi_s'; r_s, \varphi_P, 0)) + \epsilon \left. \frac{\partial \delta}{\partial g} \frac{\partial g}{\partial \epsilon} \right|_{\epsilon=0} + O(\epsilon^2), \tag{7.8}$$

where we take $g(\varphi_s'; r_s, \varphi_P, \epsilon) = r_s + \epsilon \exp(-\alpha_T(\varphi_s' - \varphi_P)^2)$.

The directivity factor $\mathscr{D}_\omega$ is then expanded to $O(\epsilon)$ which can be written as

$$\mathscr{D}_\omega \sim \mathscr{D}_\omega^{(0)} + \epsilon \mathscr{D}_\omega^{(1)}, \tag{7.9}$$

where $\mathscr{D}_\omega^{(0)}$ is equal to (**??**) and it can be shown that $\mathscr{D}_\omega^{(1)}$ is the sum of the two terms

$$\frac{1}{|\mathscr{G}_\omega|^2} \int_{-\pi}^{\pi} \mathbb{G}_\omega^*(\boldsymbol{x}_R | r_s, \varphi_s') \left. \frac{\partial g}{\partial \epsilon} \frac{\partial}{\partial g} \mathbb{G}_\omega(\boldsymbol{x}_R | g(\varphi_s'; r_s, \varphi_P, \epsilon), \varphi_s') \right|_{\epsilon=0} \mathrm{d}\varphi_s' + \mathrm{c.c} =$$

$$\frac{-\sqrt{2}\,\mathrm{i}}{\bar{c}_\infty k_0^{3/2} \Phi_s^2} \left[\sum_{n=-\infty}^{+\infty} \sum_{m=-\infty}^{+\infty} \left(\frac{\sqrt[4]{-\eta_n^{(1)}(r_s)}}{\sqrt{r_s Q_n(r_s)}} \right)^* \mathrm{Ai}\left(\eta_n^{(1)}(r_s)\right) \mathrm{e}^{-\mathrm{i}k_0 \zeta_n(r_s)} \mathscr{M}_m \mathscr{Y}(\varphi; m\text{-}n, \varphi_P, \alpha_T) \right] + \mathrm{c.c.}, \tag{7.10}$$

where

$$\mathscr{M}_m = -\frac{\mathrm{i}}{\bar{c}_\infty k_0 \Phi_s^2} \mathrm{e}^{\mathrm{i}k_0 \zeta_m(r_s)} \times \left[\frac{2^{3/2}\, \mathrm{d}\Phi_s/\mathrm{d}r_s}{k_0^{1/2} \Phi_s} \left(\frac{\sqrt[4]{-\eta_m^{(1)}(r_s)}}{\sqrt{r_s Q_m(r_s)}} \right) \mathrm{Ai}\left(\eta_m^{(1)}(r_s)\right) + \left(\frac{\sqrt{2k_0 Q_m(r_s)}}{\sqrt[4]{-r_s^2 \eta_m^{(1)}(r_s)}} \right) \frac{\mathrm{d}}{\mathrm{d}\eta_m^{(1)}} \mathrm{Ai}\left(\eta_m^{(1)}(r_s)\right) \right]. \tag{7.11}$$

The effect of the perturbations on the ring source are shown in figure **??**. This figure shows that even for small changes in the asymmetry of the source there are significant changes in the qualitative behaviour of the field. The upstream beaming is immediately recognisable as soon as the field is perturbed, with the field smoothed as in the case of the weighted ring sources. However, unlike the weighted source cases, the largest cusp related magnitudes are of the same order as the swallowtail related diffraction patterns delimiting the cone of silence. The overall impact of these overlapping swallowtail singularities is reduced with increasing α_T, with the concentration of diffraction field again resembling a point source field in its organisation.

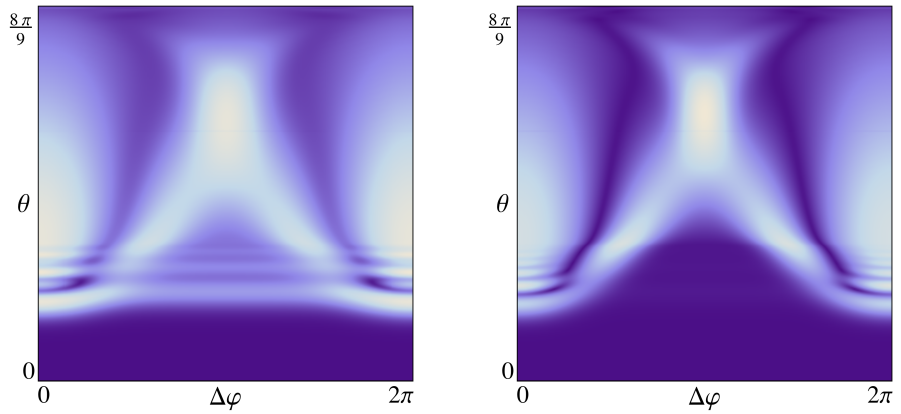

(a) $\varphi_P = \pi/2$, $\alpha_T = 2.5$, $\epsilon = 0.01$ (b) $\varphi_P = \pi/2$, $\alpha_T = 5$, $\epsilon = 0.25$

Figure 17: Field magnitude, $|\mathscr{D}_\omega|$, in $(\Delta\varphi, \theta)$ due to perturbed ring source source, using (**??**), (**??**) (**??**). Here $\Delta\varphi = \varphi - \varphi_P$ and parameters $St = 5$, $k_0 = 28.27$, $r_s = 0.75$, were used.

Given the studies undertaken in this section it is not difficult to surmise that coupling both weighted and perturbation cases together would likely see the cusp as non-negligible.

8. Conclusion

The discovery of the upstream acoustic cusp in a parallel subsonic shear flow with asymmetric source distributions provides a new perspective on how high-frequency acoustic waves propagate in jets. This fully 3D effect leads to a distinctive diffraction pattern (in the absence of any scattering from structures) with significant peak amplitude in the upstream direction. For a point source of acoustic radiation, the cusp behaves canonically being decorated locally by the Pearcey function and is formed by an interacting ray triplet creeping back against the flow.

Spurred on by this discovery we revisited the downstream field organised about a fold caustic and Schwarzschild line, the latter characterised by a radial potential of the form used in black hole theory. We resolved the interaction of these structures by performing a local analysis that introduced a new controlling form, not simply Airy as with folds, but a complex Pearcey-like function. Though appearing non-canonical, the overall controlling structure is that of a swallowtail catastrophe and is thus locally structurally stable. Not only does this new form predict cusps downstream arising from swallowtail cross-sections, explaining the kinks in the fold at large source radii, but we are also able to predict new complex ray shedding as one traverses the Schwarzschild line, with the effect of smoothing the field.

With the cusp and swallowtail structures resolved, it is a simple question of which forms dominate when the acoustic field is the product of multiple sources. While equally weighted point sources suggest the total elimination of the cusp, perturbations to a ring source, representative of the "imperfect" round jet, introduce asymmetries restoring the upstream beaming effect.

Currently, there is a lack of experimental data comprehensively covering the upstream angular regions for asymmetric source distributions in subsonic flows that form the subject of this study. As trends in aircraft design suggest closer coupling between the engine and the aircraft structures, leading to an effective asymmetry in effective acoustic source distributions, a systematic experimental study is highly desirable. If the presence of upstream caustics were to be observed, this might have practical implementations for novel jet-wing or jet-nozzle acoustic interactions in future aircraft design.

Data accessibility. Computational documents (CDFs) of Green function and ray trajectories are available within the electronic supplementary material. Additional data supporting this paper is openly available from the University of Southampton repository at http://dx.doi.org/10.5258/SOTON/403450.
Conflict of interests. We have no competing interests.
Author's contributions. All authors participated in formulation of the mathematical model and wrote the paper. J.T.S. did the numerical simulations. All authors gave final approval for publication.
Acknowledgements. The authors thank the reviewers for their valuable comments and suggestions. J.T.S. would like to thank Rolls-Royce for their support.
Funding statement. This work was supported by EPSRC [EP/M508147/1], Rolls-Royce and Mathematical Sciences (University of Southampton).

A. Extensions to simple turning-point problem

(a) Transitional & uniform forms

In this section we outline the theory used to derive the "transitional" uniform solutions valid in the vicinity of an isolated turning-point r_δ (where r_δ is any r_{δ_k} see section **??**) . By "transitional" we mean the leading order term with error of magnitude $O(k_0^{-2(1+m_{r_\delta})/(2+m_{r_\delta})})$. Further work can be found in Olver [**?**].

Starting with the radial equation

$$\frac{\mathrm{d}^2 v}{\mathrm{d}r^2} + (k_0^2 Q_n^2 + \mathscr{I})v = 0, \tag{A 1}$$

then Q_n^2 has an isolated turning-point, r_δ, of order m_{r_δ} if Q_n^2 vanishes as $Q_n^2 = O(r - r_\delta)^{m_{r_\delta}}$. One seeks a simpler function that mirrors the turning-point structure of v, but is less recondite. Making the transformations $r = r(\eta)$ and $V(\eta; k_0) = \dot{r}^{-\frac{1}{2}} v$ (where $\cdot$ denotes $\mathrm{d}/\mathrm{d}\eta$), giving

$$\ddot{V} + \left(k_0^2 \dot{r}^2 Q_n^2(r) + \widetilde{\mathscr{I}}(\eta)\right) V = 0, \tag{A 2}$$

where $\widetilde{\mathscr{I}}(\eta) = \dot{r}^2 \mathscr{I}(r) + \dot{r}^{-\frac{1}{2}}(\mathrm{d}^2 \dot{r}^{-\frac{1}{2}}/\mathrm{d}\eta^2)$. Now if we choose $\dot{r}^2 Q_n^2(r) = \eta^{m_{r_\delta}}$, then V satisfies

$$\ddot{V} + \left(k_0^2 \eta^{m_{r_\delta}} + \widetilde{\mathscr{I}}(\eta)\right) V = 0, \quad \text{with} \quad \eta = \left(\frac{m_{r_\delta}+2}{2} \int_{r_\delta}^{r} Q_n(r')\,\mathrm{d}r'\right)^{2/(m_{r_\delta}+2)}, \tag{A 3}$$

where as a first approximation, i.e., $\widetilde{\mathscr{I}} = 0$, V has two linearly independent (transitional) solutions $V_\pm$ in terms of Bessel functions $J_{\pm 1/(2+m_{r_\delta})}$

$$V_\pm(\eta; k_0) = \eta^{1/2} J_{\pm\frac{1}{2+m_{r_\delta}}}\left(\frac{2k_0\eta^{(2+m_{r_\delta})/2}}{2+m_{r_\delta}}\right) = \eta^{1/2} J_{\pm\frac{1}{2+m_{r_\delta}}}\left(k_0 \int_{r_\delta}^{r} Q_n(r')\,\mathrm{d}r'\right). \tag{A 4}$$

The full uniform asymptotics can be obtained by substitution of the series

$$V(\eta; k_0) = V_\pm(\eta; k_0) \sum_{\ell=0}^{+\infty} \frac{A_\ell}{k_0^{2\ell}} + \frac{1}{k_0^2}\frac{\mathrm{d}}{\mathrm{d}\eta} V_\pm(\eta; k_0) \sum_{\ell=0}^{+\infty} \frac{B_\ell}{k_0^{2\ell}}, \tag{A 5}$$

into (**??**), where the coefficients satisfy

$$A_{\ell+1}(\eta) = -\frac{1}{2}\dot{B}_\ell(\eta) + \frac{1}{2}\int_0^\eta \widetilde{\mathscr{I}}(\eta') B_\ell(\eta')\,\mathrm{d}\eta', \tag{A 6}$$

$$B_\ell(\eta) = \frac{1}{4\eta^{m_{r_\delta}/2}} \int_0^\eta \frac{1}{(\eta')^{m_{r_\delta}/2}} \left[\widetilde{\mathscr{I}}(\eta') A_\ell(\eta') - \ddot{A}_\ell(\eta')\right] \mathrm{d}\eta', \tag{A 7}$$

with $A_0 = \mathrm{const.}$ determined from (**??**). We then have $v = \dot{r}^{1/2} V(\eta; k_0)$, with V given by (**??**).

The Bessel functions (**??**) can be expressed in terms of Airy functions when $m_{r_\delta} = 1$ and parabolic cylinder functions when $m_{r_\delta} = 2$ (see chapter 10.16, [**?**]). In both cases it is expedient

to absorb k_0 and $(-1)^{m_{r_\delta}}$ into η of (**??**) to give

$$\eta_n^{(m_{r_\delta})}(r) \equiv (-1)^{m_{r_\delta}} \left(\frac{m_{r_\delta}+2}{2} k_0 \zeta_n(r) \right)^{2/(m_{r_\delta}+2)}. \tag{A 8}$$

The uniform forms derived here are equally applicable to radial equations evaluated at $s = r_s$ when the WKB solutions (**??**) are singular, i.e., when $r_s = r_{\delta_k}$ of section **??**.

(b) Three turning-points

In the event of three turning-points, $T = 3$, we modify the expansion of (**??**), $\eta_n^{(1)} \gg 1$,

$$v_2(r_s) \sim \gamma_{12}^{(1)} \begin{cases} \mathrm{e}^{\pi \mathrm{i}/4} Q_n^{-\frac{1}{2}}(r_s) \left(\underbrace{\exp\left(-\mathrm{i}k_0 \int_{r_{\delta_1}}^{r_s} Q_n(r')\,\mathrm{d}r' \right)}_{p.1} - \mathrm{i} \underbrace{\exp\left(+\mathrm{i}k_0 \int_{r_{\delta_1}}^{r_s} Q_n(r')\,\mathrm{d}r' \right)}_{p.2} \right), & r_s > r_{\delta_1} \\ Q_n^{-\frac{1}{2}}(r_s) \exp\left(-k_0 \int_{r_s}^{r_{\delta_1}} |Q_n(r')|\,\mathrm{d}r' \right), & r_s < r_{\delta_1} \end{cases} \tag{A 9}$$

then appealing to continuity in the modes we subdivide the two cases of the $T = 1$ problem. Note that in all cases we can solve for $v_1(r)$ by making the replacement $r_{\delta_1} \to r_{\delta_3}$ in (**??**).

The first two subcases are $r_{\delta_3} < r_s$ and $r_{\delta_2} < r_s < r_{\delta_3}$, we simply reuse (**??**) with $r_{\delta_1} \to r_{\delta_3}$, ignoring $r_{\delta_{1,2}}$. However in the subcases $r_s < r_{\delta_2}$ we must take care to integrate the phases over the regions of decay $0 < r' < r_{\delta_1}$ and $r_{\delta_2} < r' < r_{\delta_3}$. To demonstrate we use the most common subcase that occurs in figure **??** for the sources used in this paper, i.e., $r_s \geq 0.45$, in which case is $r_{\delta_1} < r_s < r_{\delta_2}$. Each phase must acquire a decaying factor from integration over $r_{\delta_2} < r' < r_{\delta_3}$ and this is easily accounted for in phase $p.1$ of (**??**) by replacing $r_{\delta_1} \to r_{\delta_2}$, and in phase $p.2$ by integrating from r_s to r_{δ_1} and then from r_{δ_1} to r_{δ_2}. This leads to

$$\frac{v_1(r) v_2(r_s)}{\gamma_{21}^{(2)} \gamma_{12}^{(1)}} \sim Q_n^{-\frac{1}{2}}(r_s) \left(\mathrm{e}^{-\mathrm{i}k_0 \int_{r_{\delta_2}}^{r_s} Q_n(r')\,\mathrm{d}r'} - \mathrm{i}\mathrm{e}^{\mathrm{i}k_0 \left(2\int_{r_{\delta_1}}^{r_s} Q_n(r')\,\mathrm{d}r' + \int_{r_s}^{r_{\delta_2}} Q_n(r')\,\mathrm{d}r' \right)} \right) \times \mathrm{e}^{\mathrm{i}k_0 \left(\int_{r_{\delta_3}}^{r} Q_n(r')\,\mathrm{d}r' + \mathrm{i}\int_{r_{\delta_2}}^{r_{\delta_3}} Q_n(r')\,\mathrm{d}r' \right)}, \tag{A 10}$$

where $\exp(-k_0 \int_{r_{\delta_2}}^{r_{\delta_3}} Q_n(r')\,\mathrm{d}r')$ is the new decay factor. Extensions can be derived for $r_s < r_{\delta_1}$.

B. Poisson summation and saddle point asymptotics

The Poisson summation introduced by [**?**] recasts (**??**) by decomposing (**??**) according to

$$\mathscr{R}_\omega \sim \mathscr{R}_\omega^{(-)} - \mathrm{i}\mathscr{R}_\omega^{(+)}, \tag{A 1}$$

using (**??**) and the unfolded behaviour of (**??**), i.e., (**??**) with $r_s > r_\delta = r_{\delta_1}$, for the radial solutions. This gives

$$\mathscr{R}_\omega^{(\pm)} = \sum_{m=-\infty}^{+\infty} \int_{\mathscr{C}^{(\pm)}} \left(\frac{\mathrm{i}k_0}{2\pi r_s Q(r_s|\nu)} \right)^{1/2} \mathrm{e}^{\mathrm{i}k_0 \left(\alpha_m \nu + \zeta(r|\nu) \pm \zeta(r_s|\nu) - R\sin^2\theta \right)} \mathrm{d}\nu. \tag{A 2}$$

Here the variable $\nu = n/k_0$ and function $\alpha_m = \Delta\varphi + 2\pi m$ of the Poisson index m have been introduced, along with notational changes $\zeta_n(s) \to \zeta(s|\nu)$, $Q_n(s) \to Q(s|\nu)$, where s is defined in (**??**). We use $\mathscr{C}^{(\pm)}$ as contours from 0 to an adjacent valley of $+\infty$ for saddle computations, whereas full numeric calculations of $\mathscr{R}_\omega^{(\pm)}$ should use those defined in [**?**].

The saddle point expansion of (**??**) is given as

$$\mathscr{R}_{\omega}^{(\pm)} \sim \sum_{\nu_\star} \left(r_s Q(r_s|\nu_\star) \frac{\partial \psi}{\partial \nu_\star} \right)^{-1/2} \mathrm{e}^{\mathrm{i}k_0(\alpha_{m_\star}\nu_\star + \zeta(r|\nu_\star) \pm \zeta(r_s|\nu_\star) - R\sin^2\theta)}, \tag{A 3}$$

where $\nu_\star$ are saddle-points satisfying the saddle-point condition

$$\alpha_{m_\star} = \Delta\varphi + 2\pi m_\star = \left(\int_{r_\delta}^{+\infty} \pm \int_{r_\delta}^{r_s} \right) \frac{\nu_\star \, \mathrm{d}r'}{r'^2 Q(r'|\nu_\star)} = \psi(\nu_\star), \tag{A 4}$$

and

$$\frac{\partial \psi}{\partial \nu_\star} = \frac{\psi(\nu_\star)}{\nu_\star} + 2\nu_\star^2 \left(\int_{r_\delta}^{+\infty} \mp \int_{r_\delta}^{r_s} \right) \frac{\mathrm{d}\mathscr{P}(r')/\mathrm{d}r'}{r' Q(r'|\nu_\star)} \, \mathrm{d}r' \pm \frac{2\nu_\star^2 \mathscr{P}(r_s)}{r_s Q(r_s|\nu_\star)}, \quad \mathscr{P}(r) = \frac{1}{r \, \mathrm{d}(rq)^2/\mathrm{d}r}. \tag{A 5}$$

References

1. Lighthill MJ. 1952 On sound generated aerodynamically. I. General theory. *Proc. R. Soc. Lond. A* **211**, 564–587. (doi:10.1098/rspa.1952.0060)
2. Lighthill MJ. 1954 On sound generated aerodynamically. II. Turbulence as a source of sound. *Proc. R. Soc. Lond. A* **222**, 1–32. (doi:10.1098/rspa.1954.0049)
3. Lilley GM. 1958 On the noise from air jets. *Aeronaut. Res. Council Rep. Mem.* **20**, 376.
4. Goldstein ME. 1976 *Aeroacoustics*. New York, NY: McGraw-Hill.
5. Tester BJ, Morfey CL. 1976 Developments in jet noise modelling—theoretical predictions and comparisons with measured data. *J. Sound Vib.* **46**, 79–103.
6. Wundrow DW, Khavaran A. 2004 On the applicability of high-frequency approximations to Lilley's equation. *J. Sound Vib.* **272**, 793–830. (doi:10.1016/S0022-460X(03)00420-6)
7. Bender CM, Orszag SA. 1978 *Advanced mathematical methods for scientists and engineers*. New York, NY: McGraw-Hill.
8. Mani R, Gliebe PR, Balsa TF. 1978 High velocity jet noise source location and reduction. *Fed. Aviation Admin. Rep., FAA-RD-76-II.*
9. Pierce AD, et al. 1981 *Acoustics: an introduction to its physical principles and applications*. New York, NY: McGraw-Hill.
10. Keller JB. 1978 Rays, waves and asymptotics. *Bull. Amer. Math. Soc.* **84**, 727–750.
11. Stone JT, Self RH, Howls CJ. 2014 A Complex Ray-Tracing Tool for High-Frequency Mean-Field Flow Interaction Effects in Jets. In *20th AIAA/CEAS Aeroacoustics Conf., Atlanta, GA, 16-20 June, 2014.* AIAA-2014-2757. (doi:10.2514/6.2014-2757)
12. Stone JT, Self RH, Howls CJ. 2016 Cones of silence, complex rays, & catastrophes: high-frequency acoustic analogies. In Preparation.
13. Chapman SJ, Lawry JMH, Ockendon JR, Tew RH. 1999 On the theory of complex rays. *SIAM Rev.* **41**, 417–509. (doi:10.1137/S0036144599352058)
14. Goldstein ME. 1991 Noise from Turbulent Shear Flows. In: Hubbard HH. ed. *Aeroacoustics of flight vehicles: Theory and practice. Volume 1. Noise sources*. DTIC document, pp. 291–310.
15. Berry MV, Upstill C. 1980 Catastrophe optics: morphologies of caustics and their diffraction patterns. *Prog. Opt.* **18**, 257–346.
16. Olver FWJ, Olde Daalhuis AB, Lozier DW, Schneider BI, Boisvert RF, Clark CW, Miller BR, Saunders BV. *NIST Digital Library of Mathematical Functions*. Release 1.0.13 of 2016-09-16. Available from http://dlmf.nist.gov.
17. Poston T, Stewart I. 2014 *Catastrophe theory and its applications*. Mineola, NY: Dover.
18. Thom R. 1989 *Structural stability and morphogenesis*. Advanced Books Classic Series. Boston, MA: Addison-Wesley.
19. Powell A. 1953 On the mechanism of choked jet noise. *Proc. Phys. Soc. B* **66**, 1039–1056.
20. Norum TD, Seiner, JM. 1982 Broadband shock noise from supersonic jets. *AIAA J.* **20**, 68–73. (doi:10.2514/3.51048)
21. Kandula M. 2008 On the scaling laws and similarity spectra for jet noise in subsonic and supersonic flow. *Int. J. Acoust. Vib.* **13**, 3–16.
22. Powles CJ, Tester, BJ. 2008 Asymptotic and Numerical Solutions for Shielding of Noise Sources by Parallel Coaxial Jet Flows. In *14th AIAA/CEAS Aeroacoustics Conf., Vancouver, BC, 5-7 May, 2008.* AIAA-2008-2975. (doi:10.2514/6.2008-2975)

23. Abrahams ID, Kriegsmann GA, Reiss EL. 1989 On the development of caustics in shear flows over rigid walls. *SIAM J. Appl. Math.* **49**, 1652–1664. (doi:10.1137/0149100)
24. Chapman, CJ. 1999 Caustics in cylindrical ducts. *Proc. R. Soc. Lond. A* **455**, 2529–2548. (doi:10.1098/rspa.1999.0415)
25. Coulouvrat F. 2000 Focusing of weak acoustic shock waves at a caustic cusp. *Wave motion* **32**, 233–245.
26. Shariff K, Manning TA. 2013 A ray tracing study of shock leakage in a model supersonic jet. *Phys. Fluids* **25**. (doi:10.1063/1.4813630)
27. Goldstein ME. 1982 High frequency sound emission from moving point multipole sources embedded in arbitrary transversely sheared mean flows. *J. Sound Vib.* **80**, 499–522. (doi:10.1016/0022-460X(82)90495-3)
28. Duffy DG. 2001 *Green's functions with applications*. Boca Raton, FL: CRC Press.
29. Bleistein N, Handelsman RA. 1986 *Asymptotic Expansions of Integrals*. Mineola, NY: Dover.
30. Heading J. 1962 Phase-integral methods I. *Q. J. Mech. Appl. Math.* **15**, 215–244.
31. Andersson N, Howls CJ. 2004 The asymptotic quasinormal mode spectrum of non-rotating black holes. *Classical Quant. Grav.* **21**, 1623.
32. Powles CJ, Tester BJ, McAlpine A. 2010 A weak-scattering model for turbine-tone haystacking outside the cone of silence. *Int. J. Aeroacoust.* **10**, 17–50.
33. Ring JD, Lindberg J, Howls CJ, Dennis MR. 2012 Aberration-like cusped focusing in the post-paraxial Talbot effect. *Journal of Optics* **14**, 075702. (doi:10.1088/2040-8978/14/7/075702)
34. Bleistein N. 1967 Uniform asymptotic expansions of integrals with many nearby stationary points of algebraic singularities. *J. Math. Mech.* **17**, 533–559.
35. Stone JT, Self RH, Howls CJ. 2017 Invisible catastrophes when to turn a blind eye. In preparation.
36. Smith MJT. 2004 *Aircraft noise*. Cambridge, UK: Cambridge University Press.
37. Khavaran A, Georgiadis NJ, Bridges J, Dippold VF. 2005 Effect of free jet on refraction and noise. In *11th AIAA/CEAS Aeroacoustics Conf., Monterey, CA, 23-25 May, 2005*. AIAA-2005-2941.
38. Morris PJ, Farassat F. 2002 Acoustic analogy and alternative theories for jet noise prediction. *AIAA J.* **40**, 671–680.
39. Self RH. 2004 Jet noise prediction using the Lighthill acoustic analogy. *J. Sound Vib.* **275**, 757–768.
40. Olver FWJ. 1974 *Asymptotics and special functions*. New York, NY: Academic Press.